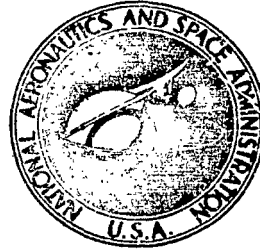


NASA TECHNICAL NOTE



NASA TN D-7195

NASA TN D-7195

TECH LIBRARY KAFB, NM
0133523
LOAN CO
AFWL TE
KIRTLAN

(NASA-TN-D-7195) CALCULATION OF ENERGY
DEPOSITION DISTRIBUTIONS FOR SIMPLE
GEOMETRIES (NASA) 66 p HC \$3.00

N73-17832

CSCI. 03B

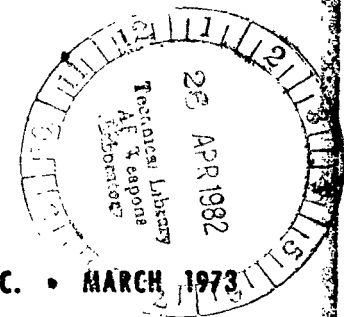
Unclass

H1/29 63419

**CALCULATION OF ENERGY DEPOSITION
DISTRIBUTIONS FOR SIMPLE GEOMETRIES**

by John W. Watts, Jr.

*George C. Marshall Space Flight Center
Marshall Space Flight Center, Ala. 35812*





0133523

1. Report No. NASA TN D-7195		2. Government Accession No.		3. Recipient's Catalog No.	
4. Title and Subtitle Calculation of Energy Deposition Distributions for Simple Geometries				5. Report Date March 1973	
				6. Performing Organization Code	
7. Author(s) John W. Watts, Jr.				8. Performing Organization Report No. M452	
9. Performing Organization Name and Address George C. Marshall Space Flight Center Marshall Space Flight Center, Alabama 35812				10. Work Unit No.	
				11. Contract or Grant No.	
12. Sponsoring Agency Name and Address National Aeronautics and Space Administration Washington, D.C.				13. Type of Report and Period Covered Technical Note	
				14. Sponsoring Agency Code	
15. Supplementary Notes Prepared by Space Sciences Laboratory, Science and Engineering					
16. Abstract <p>When high-energy charged particles pass through a thin-detector, the ionization energy loss in that detector is subject to fluctuations or "straggling" which must be considered in interpreting the data. This problem has been treated by Landau, Symon, Vavilov, and others. Under many conditions, which depend upon the charge and energy of the incident particle and the detector geometry, the ionization energy lost by the particle is significantly different from the energy deposited in the detector. Since most detectors respond according to the ionization energy deposited, the difference between energy lost in the detector and energy deposited there must be considered. This difference is caused by high-energy secondary electrons produced in the ionization process that travel far from their point of production, often leaving the detector.</p> <p>This problem divides naturally into a calculation of the energy loss that results in excitation and low-energy secondary electrons which do not travel far from their production points, and a calculation of energy loss that results in high-energy secondary electrons which can escape from the detector.</p> <p>The first calculation is performed using a modification of the Vavilov energy loss distribution. A cutoff energy is introduced above which all electrons are ignored and energy transferred to low energy particles is assumed to be equivalent to the energy deposited by them.</p> <p>For the second calculation, the trajectory of the primary particle is considered as a source of secondary high-energy electrons. The electrons from this source are transported using Monte Carlo techniques and multiple scattering theory, and the energy deposited by them in the detector is calculated. The results of the two calculations are then combined to predict the energy deposition distribution.</p> <p>The results of these calculations are used to predict the charge resolution of parallel-plate pulse ionization chambers that are being designed to measure the charge spectrum of heavy nuclei in the galactic cosmic-ray flux.</p>					
17. Key Words (Suggested by Author(s))			18. Distribution Statement		
19. Security Classif. (of this report) Unclassified		20. Security Classif. (of this page) Unclassified		21. No. of Pages 65	22. Price* \$5.00



PRECEDING PAGE BLANK NOT FILMED

TABLE OF CONTENTS

	Page
I. INTRODUCTION	1
II. THE DISTRIBUTION OF ENERGY LOST DUE TO LOW ENERGY TRANSFERS	3
A. Development of the Restricted Energy-Loss Distribution	3
B. Results for the Restricted Energy-Loss Distribution	13
III. HIGH-ENERGY DELTA-RAY DISTRIBUTION	13
IV. HIGH-ENERGY, DELTA-RAY TRANSPORT AND ENERGY DISPOSITION	17
V. TOTAL ENERGY DEPOSITION	24
VI. RESULTS AND CONCLUSIONS	25
APPENDIX A. DERIVATION OF THE ANGLE - ENERGY RELATIONSHIP FOR DELTA-RAY PRODUCTION AND THE EQUATION FOR MAXIMUM TRANSFERABLE ENERGY	44
APPENDIX B. SAMPLING FROM FREQUENCY DISTRIBUTION	48
APPENDIX C. THE MOLIERE MULTIPLE SCATTERING DISTRIBUTION	50
APPENDIX D. USE OF DIRECTION COSINES FOR DESCRIBING PARTICLE SCATTERING	53
APPENDIX E. DERIVATION OF THE CONTINUITY EQUATION OF THE ENERGY-LOSS FREQUENCY DISTRIBUTION	56
REFERENCES	59

LIST OF ILLUSTRATIONS

Figure		Page
1.	Restricted energy loss distribution with various delta-ray energy cutoffs for an iron nucleus (Fe^{56}) with an energy of 2.5 GeV/nucleon for a pathlength of 5.1 cm in a mixture of 90-percent argon and 10-percent methane at 1 atmosphere of pressure ϵ_{max} was 12.853 Mev	14
2.	Energy loss distribution due to delta rays with energies above 0.80 MeV for an iron nucleus (Fe^{56}) with an energy of 2.5 GeV/nucleon for a pathlength of 5.1 cm in a mixture of 90-percent argon and 10-percent methane at 1 atmosphere of pressure	16
3.	Total energy loss distribution calculated using the convolution integral [equation (24)] on the distribution shown in Figure 2 and the corresponding distribution ($\epsilon_1 = 0.08$ MeV) from Figure 1	18
4.	Energy deposition for 0.5 MeV electron normally incident on an aluminum slab	20
5.	Energy deposition for 1.0 MeV electron normally incident on an aluminum slab	21
6.	Energy deposition for 4.0 MeV electrons normally incident on an aluminum slab	22
7.	Geometry for high energy electron production and scattering showing electrons produced inside and exterior to the chamber	23
8.	Calculated frequency distribution of energy deposition in the first of two stacked ionization counters of Israel et al. [1] by iron nuclei (Fe^{56}) normally incident at 2.5 GeV/nucleon.	26
9.	Calculated frequency distribution of energy deposition in the second of two stacked ionization counters of Israel et al. [1] by iron nuclei (Fe^{56}) normally incident at 2.5 GeV/nucleon.	27
10.	Comparison of Israel et al. [1] results with our calculated distribution including noise and contribution from charges 25 and 27.	28
11.	The energy deposition frequency distribution for iron (Fe^{56}) nuclei normally incident at 2.5 GeV/nucleon on a bare slab with dimensions 99 x 99 x 5.1 cm composed of 90-percent argon and 10-percent methane at a pressure of 1 atmosphere	30

LIST OF ILLUSTRATIONS (Continued)

Figure		Page
12.	The energy deposition frequency distribution for nitrogen (N^{14}) nuclei normally incident at 10.0 GeV/nucleon on the four-chamber instrument. (These results are for the first two-chamber-coupled detector.)	31
13.	The energy deposition frequency distribution for nitrogen (N^{14}) nuclei normally incident at 10.0 GeV/nucleon on the four-chamber instrument. (These results are for the second two-chamber-coupled detector.)	32
14.	The energy deposition frequency distribution for oxygen (O^{16}) nuclei normally incident at 10.0 GeV/nucleon on the four-chamber instrument. (These results are for the first two-chamber-coupled detector.)	33
15.	The energy deposition frequency distribution for oxygen (O^{16}) nuclei normally incident at 10.0 GeV/nucleon on the four-chamber instrument. (These results are for the second two-chamber-coupled detector.)	34
16.	The energy deposition frequency distribution for sulfur (S^{32}) nuclei normally incident at 10.0 GeV/nucleon on the four-chamber instrument. (These results are for the first two-chamber-coupled detector.)	35
17.	The energy deposition frequency distribution for sulfur (S^{32}) nuclei normally incident at 10.0 GeV/nucleon on the four-chamber instrument. (These results are for the second two-chamber-coupled detector.)	36
18.	The energy deposition frequency distribution for chromium (Cr^{52}) nuclei normally incident at 10.0 GeV/nucleon on the four-chamber instrument. (These results are for the first two-chamber-coupled detector.)	37
19.	The energy deposition frequency distribution for chromium (Cr^{52}) nuclei normally incident at 10.0 GeV/nucleon on the four-chamber instrument. (These results are for the second two-chamber-coupled detector.)	38
20.	The energy deposition frequency distribution for manganese (Mn^{55}) nuclei normally incident at 10.0 GeV/nucleon on the four-chamber instrument. (These results are for the first two-chamber-coupled detector.)	39

LIST OF ILLUSTRATIONS (Concluded)

Figure		Page
21.	The energy deposition frequency distribution for manganese (Mn^{55}) nuclei normally incident at 10.0 GeV/nucleon on the four-chamber instrument. (These results are for the second two-chamber-coupled detector.).....	40
22.	The energy deposition frequency distribution for iron (Fe^{56}) nuclei normally incident at 10.0 GeV/nucleon on the four-chamber instrument. (These results are for the first two-chamber-coupled detector.).....	41
23.	The energy deposition frequency distribution for iron (Fe^{56}) nuclei normally incident at 10.0 GeV/nucleon on the four-chamber instrument. (These results are for the second two-chamber-coupled detector.).....	42

CALCULATION OF ENERGY DEPOSITION DISTRIBUTIONS FOR SIMPLE GEOMETRIES

I. INTRODUCTION

Parallel plate ionization chambers are to be used [1] as part of an instrument to measure the charge spectrum of heavy nuclei in the galactic cosmic-ray flux. The ionization chamber measurement determines the energy deposited by the cosmic ray along its trajectory through the chamber while other portions of the instrument determine the distance traveled through the chamber. (The trajectory is approximately a straight line unless the cosmic ray has a nuclear interaction.) From these two measurements, the energy deposited in the chamber per unit pathlength of the cosmic ray can be determined. The stopping power or mean energy lost per unit pathlength in material - dT/dx is directly related to the incident particle's charge. For nuclei up to about iron, calculations of stopping power based on the first Born approximation appear to be valid [2,3]. These calculations predict that the stopping power is proportional to the nuclear charge squared. For nuclei above iron, higher terms in the perturbation theory series must be taken or a partial wave expansion must be used [3,4] to derive the charge-stopping power relationship.

However, the stopping power gives us only the average energy lost by the particle in the detector. A beam of particles of the same trajectory, charge, and energy will produce a distribution of energy losses in the ionization chamber. This fluctuation in energy loss in a thin absorber, sometimes called "straggling," is the result of the finite number of events that occur in the ionization energy loss process. Energy transfer to the electrons in the absorber material produces excitation and ionization. Many of the electrons gain considerable energy. The probability of large energy transfers, which depends upon the impact parameter in the classical picture, becomes smaller with higher secondary electron energy so that the fluctuations in the number of events become greater at higher energies. As a result, the energy loss distribution for fast charged particles in thin absorbers has a considerable width and is skewed to the high energy side. The problem of calculating this distribution was first attacked theoretically by Landau [5] for thin absorbers where only a small fraction of the particle's initial energy is lost. He used Laplace transforms to solve the continuity equation of the distribution function of energy loss. In addition to the assumption that the energy loss was small, his derivation places no upper limit on the energy transferred to a single electron of the absorber. This approximation limited the validity of his solution to electrons, positrons, and heavy particles of very high energy or in very thin absorbers. Symon [6] solved the problem more generally by using numerical techniques both for thin absorbers where the average energy loss was less than 10 percent of the initial energy and for thick absorbers where the average energy loss is more than 10 percent of the initial energy. Vavilov [7] followed Landau's basic approach, but he obtained a more rigorous solution without the approximation of unbounded single energy transfers. Thus, his results could be applied to a wider range of particles and energies though still restricted to thin absorbers. We will use Vavilov's general method of solution extensively in Section II.

For a typical primary cosmic ray with kinetic energy in the GeV/nucleon range, a number of energy loss mechanisms are available - scattering of electrons (delta rays), excitation of atomic electrons to higher bound-energy states, production of Cerenkov radiation (the radiation produced when a particle passes through a dielectric at a velocity faster than the phase velocity of light in the medium) [8], and production of bremsstrahlung radiation (radiation that is produced when a charged particle undergoes acceleration). Production of delta rays and excitation is the most important energy loss process contributing to the total stopping power for the particles considered here. Cerenkov losses are responsible for only a small fraction of the relativistic rise of the stopping power [9], and bremsstrahlung losses are negligible because of the high mass of the nuclei. We will confine ourselves to consideration of the interactions with electrons.

Cosmic rays can also undergo nuclear interactions with the chamber material. Waddington et al. [10] have measured the interaction mean free path for cosmic rays in nuclear emulsions. Their results show that the mean free path varies, with minor energy dependence (energy range was 100 MeV/nucleon to 30 GeV/nucleon), from about 19 cm of emulsion (the equivalent of about 46 g/cm² of air) for alpha particles to about 10 cm of emulsion (27 g/cm² of air) for very heavy primaries with nuclear charges greater than 20. Because the ionization chambers considered here are relatively thin ($x < 1.0$ g/cm²) compared with the interaction mean free path, few nuclear interactions will occur, and they are identified by the trajectory measurement in the experiment [1] and treated separately.

The problem to be attacked here is the result of the subtle distinction between the energy lost in a given element of volume along the cosmic ray's path and the energy deposited there, since energy can be transported in and out of the volume element by secondary particles and radiation. Thus, energy loss depends on the type of material in the volume, whereas energy deposited depends on the surrounding geometry as well. Since delta rays transport practically all energy that is removed from the region where it is lost by the primary particle, let us consider how geometry affects their production, transport, and energy deposition. For a small region on the path of a heavy cosmic ray through a piece of material, the production of a high-energy delta ray will cause a large fluctuation in the energy lost in the region; but, since the delta ray will leave the region with little energy loss, the fluctuation in energy deposition will not be as large. Conversely, electrons from other portions of the path may scatter into the region, contributing to energy deposition in the region. More of the energy of lower-energy delta rays is deposited in the region of production. Finally, at some delta-ray energy, depending on the size and shape of the region, energy loss is equivalent to energy deposition because few of the delta rays escape from the region relative to the number produced there.

Even if the relationship between the mean energy deposition and charge was known, problems would exist because the production and transport of the delta rays are random processes and the energy deposited in a region by identical cosmic rays will fluctuate from event to event depending on the number and energies of the delta rays produced. For an ionization chamber, this results in an uncertainty in the determination of the exact charge of the cosmic ray. Thus, the interesting quantity that we will attempt to calculate here is the frequency distribution of energy deposition by a heavy cosmic ray considering the fluctuations in delta-ray production and transport.

To attack the delta-ray problem, we will use the procedure of dividing it into two problems according to the delta-ray energy. The breaking-point energy ϵ_1 is selected to meet two criteria. First, it must be large compared with the binding energy of electrons in the material so that electrons scattered at energies above this energy may be treated as free electrons for the scattering cross-section calculation. This places a lower bound on ϵ_1 in the 10- to 100-KeV range [11]. Second, since we will assume that all electrons with energies below ϵ_1 deposit their energy in the volume element where they are produced, so that energy loss is equivalent to energy deposition, the distance that electrons with energies below ϵ_1 can travel must be on the order of the smallest dimension of the production volume element. For the calculation shown here, ϵ_1 was 80 or 100 KeV because the ionization chambers considered are relatively thin. For other geometries, ϵ_1 could be much higher.

We will calculate the energy-loss/deposition distribution caused by low-energy delta rays and excitation using a modification of the Vavilov energy-loss distribution [7] to be derived here. The modification consists of introducing a cutoff energy above which all delta rays are ignored. For the delta rays above ϵ_1 , we will calculate the production number and energy distribution, and then determine energy deposited in the detector by these electrons using Monte-Carlo techniques. Since delta rays produced in the chamber electrodes and other parts of the instrument can scatter into the chamber gas, the Monte-Carlo transport will consider delta rays produced throughout the instrument.

II. THE DISTRIBUTION OF ENERGY LOST DUE TO LOW ENERGY TRANSFERS

A. Development of the Restricted Energy-Loss Distribution

The distribution of energy loss due to low energy transfers is derived in this section. The derivation shown here follows Vavilov's original derivation of the energy-loss distribution [7] where all energy transfers were considered. Here, we exclude high-energy transfers by the introduction of a cutoff energy ϵ_1 . As we will show, the introduction of the cutoff energy in the derivation is not equivalent to replacing the maximum transferable energy in the Vavilov distribution equation by a lower energy.

If we define $f(X, \Delta)d\Delta$ as the probability of an energy loss between energy Δ and $\Delta + d\Delta$ because of interactions which result in losses below ϵ_1 for particles traveling a distance X and $\omega(E, \epsilon)d\epsilon$ as the probability per unit length of an energy loss ϵ by the particle at energy E , then the continuity equation for $f(X, \Delta)$ is

$$\frac{\partial f(X, \Delta)}{\partial X} = \int_0^b \omega(E, \epsilon) f(X, \Delta - \epsilon) d\epsilon - \int_0^{\epsilon_1} \omega(E, \epsilon) f(X, \Delta) d\epsilon \quad (1)$$

[See Appendix E for a derivation of equation (1).] We assume that $E \gg \Delta$ so that $\omega(E, \epsilon)$ does not change as a function of E along the particle path. ϵ_1 is the cutoff energy above which the delta rays are ignored. It is assumed that $\omega(E, \epsilon) = 0$ for $\epsilon > \epsilon_1$. Thus, b is equal to Δ for $\Delta < \epsilon_1$ and equal to ϵ_1 for $\Delta > \epsilon_1$.

To use Laplace transforms on equation (1), we note that

$$\begin{aligned} \phi(X, P) &\equiv P \int_0^{\infty} e^{-P\Delta} f(X, \Delta) d\Delta \\ f(X, \Delta) &= \frac{1}{2\pi i} \int_{C-i\infty}^{C+i\infty} \frac{e^{P\Delta} \phi(X, P)}{P} dP \\ \psi(E, P) &\equiv P \int_0^{\infty} e^{-P\epsilon} \omega(E, \epsilon) d\epsilon \\ \omega(E, \epsilon) &= \frac{1}{2\pi i} \int_{C-i\infty}^{C+i\infty} \frac{e^{P\epsilon} \psi(E, P)}{P} dP \end{aligned} \tag{2}$$

where C is an arbitrary constant. When b equals Δ , using the convolution theorem on the first term on the right of equation (1), we obtain

$$\frac{\partial \phi(X, P)}{\partial X} = \frac{\psi(E, P) \phi(X, P)}{P} - \phi(X, P) \int_0^{\epsilon_1} \omega(E, \epsilon) d\epsilon \tag{3}$$

Solving the differential equation, we get

$$\phi(X, P) = \phi(0, P) \exp \left\{ \left[\frac{\psi(E, P)}{P} - \int_0^{\epsilon_1} \omega(E, \epsilon) d\epsilon \right] X \right\} \tag{4}$$

$$\frac{\psi(E, P)}{P} = \int_0^{\epsilon_1} e^{-P\epsilon} \omega(E, \epsilon) d\epsilon \quad ;$$

thus,

$$\phi(X, P) = \phi(0, P) \exp \left\{ \left[\int_0^{\xi_1} e^{-P\epsilon} \omega(E, \epsilon) d\epsilon - \int_0^{\xi_1} \omega(E, \epsilon) d\epsilon \right] X \right\}. \quad (5)$$

The incident particles will have no losses; thus,

$$f(0, \Delta) = \delta(\Delta)$$

• where $\delta(\Delta)$ is the Dirac delta function and

$$\begin{aligned} \phi(0, P) &= P \int_0^{\infty} e^{-P\Delta} \delta(\Delta) d\Delta \\ &= P \end{aligned}$$

By transforming equation (5), we have

$$\begin{aligned} f(X, \Delta) &= \frac{1}{2\pi i} \int_{C-i\infty}^{C+i\infty} \frac{e^{P\Delta}}{P} \left\{ P \exp \left\{ \left[\int_0^{\xi_1} e^{-P\epsilon} \omega(E, \epsilon) d\epsilon \right. \right. \right. \\ &\quad \left. \left. \left. - \int_0^{\xi_1} \omega(E, \epsilon) d\epsilon \right] X \right\} \right\} dP \end{aligned} \quad (6)$$

or

$$f(X, \Delta) = \frac{1}{2\pi i} \int_{C-i\infty}^{C+i\infty} \exp \left[\Delta P + X \int_0^{\epsilon_1} \omega(E, \epsilon) (e^{-P\epsilon} - 1) d\epsilon \right] dP \quad (7)$$

For b equal ϵ_1 , we get the same equation because of the way $\omega(E, \epsilon)$ is defined. This is basically Vavilov's form of the expression except that in his case ϵ_1 is the maximum transferable energy. We may rewrite the exponent in equation (7) as

$$I = P \left[\Delta - X \int_0^{\epsilon_1} \epsilon \omega(E, \epsilon) d\epsilon \right] + X \int_0^{\epsilon_1} \omega(E, \epsilon) (e^{-P\epsilon} + P\epsilon - 1) d\epsilon \quad (8)$$

where distant collisions between the particles and electrons play an important role in the first term only. The integral in the first term can be written as

$$I_1 = \int_0^{\epsilon_{\max}} \epsilon \omega(E, \epsilon) d\epsilon - \int_{\epsilon_1}^{\epsilon_{\max}} \epsilon \omega(E, \epsilon) d\epsilon \quad (9)$$

where ϵ_{\max} is the maximum possible energy transferred to an electron given by

$$\epsilon_{\max} = \frac{mc^2 \beta^2 \gamma^2}{1 + \frac{2m}{M} + \left(\frac{m}{M}\right)^2}$$

Here, m is the electron mass, c is the speed of light, β is the primary particle velocity over c , M is the primary particle mass, and γ is defined as

$$\gamma = \frac{1}{\sqrt{1 - \beta^2}}$$

(Appendix A shows a derivation of ϵ_{\max} .) The first term in equation (9) is recognized as the definition of collision stopping power $S(E)$. Thus,

$$I = P \left\{ \Delta - X \left[S(E) - \int_{\epsilon_1}^{\epsilon_{\max}} \omega(E, \epsilon) d\epsilon \right] \right\} + X \int_0^{\epsilon_1} \omega(E, \epsilon) (e^{-P\epsilon} + P\epsilon - 1) d\epsilon \quad (10)$$

If we confine ourselves to heavy energetic charged particles, we may use the results that have been obtained for $\omega(E, \epsilon)$ by applying the first-born approximation if ϵ_1 is assumed to be high enough above the electron binding energy in the first-term integral. The probability per unit pathlength for the production of an electron with energy ϵ is given by [12]

$$\omega(E, \epsilon) = \frac{2\pi NZ^2 e^4}{mc^2 \beta^2 \epsilon^2} \left(1 - \frac{\beta^2 \epsilon}{\epsilon_{\max}} \right) \quad (11)$$

where N is the number of electrons per unit volume, Z is the atomic number of the primary particle, and e is the electron charge. Defining ξ as

$$\xi \equiv \frac{2\pi NZ^2 e^4}{mc^2 \beta^2} \quad (12)$$

and substituting equation (11) into equation (1) we have

$$I = P \left[\Delta - X S(E) - \xi \int_{\epsilon_1}^{\epsilon_{\max}} \frac{1}{\epsilon} \left(1 - \frac{\beta^2 \epsilon}{\epsilon_{\max}} \right) d\epsilon \right] + X \xi \int_0^{\epsilon_1} \frac{1}{\epsilon^2} \left(1 - \frac{\beta^2 \epsilon}{\epsilon_{\max}} \right) (e^{-P\epsilon} + P\epsilon - 1) d\epsilon \quad (13)$$

Performing some of the integrals and replacing $X S(E)$, which is the mean energy loss, with $\bar{\Delta}$, we obtain

$$I = P \left[\Delta - \bar{\Delta} + X \xi \left(\ln \frac{\epsilon_{\max}}{\epsilon_1} - \beta^2 + \frac{\beta^2 \epsilon_1}{\epsilon_{\max}} \right) \right] \\ + X \xi \left[\frac{1 - e^{-\epsilon_1 P}}{\epsilon_1} - P \left(1 + \frac{\beta^2 \epsilon_1}{\epsilon_{\max}} \right) + \left(P + \frac{\beta^2}{\epsilon_{\max}} \right) \int_0^{\epsilon_1} \frac{1 - e^{-\epsilon P}}{\epsilon} d\epsilon \right]$$

Simplifying slightly and noting that [13]

$$\int_0^{\epsilon_1} \frac{1 - e^{-\epsilon P}}{\epsilon} d\epsilon = \zeta + \ln \epsilon_1 P - E_1(-\epsilon_1 P)$$

where ζ is Euler's constant 0.577 ... and $E_1(-\epsilon_1 P)$ is the exponential integral, we obtain

$$I = P \left[\Delta - \bar{\Delta} - X \xi \left(\ln \frac{\epsilon_1}{\epsilon_{\max}} + \beta^2 + 1 - \zeta \right) \right] \\ + X \xi \left\{ \left(\frac{1}{\epsilon_1} + \frac{\beta^2 \zeta}{\epsilon_{\max}} \right) - \frac{e^{-\epsilon_1 P}}{\epsilon_1} + \left(P + \frac{\beta^2}{\epsilon_{\max}} \right) \left[\ln \epsilon_1 P - E_1(-\epsilon_1 P) \right] \right\}$$

Letting

$$y = \epsilon_1 P \quad ,$$

$$\kappa = \frac{X \xi}{\epsilon_1} \quad ,$$

and

$$\lambda = \frac{\Delta - \bar{\Delta}}{\epsilon_1} - \kappa \left(\ln \frac{\epsilon_1}{\epsilon_{\max}} + \beta^2 + 1 - \xi \right) \quad (14)$$

and substituting into equation (7), we obtain

$$f(X, \Delta) = \frac{1}{2\pi \epsilon_1 i} \int_{C'}^{C'+\infty} \exp \left\{ \lambda Y + \kappa \left\{ \left(1 + \frac{\epsilon_1 \beta^2 \xi}{\epsilon_{\max}} \right) - e^{-Y} \right. \right. \\ \left. \left. + \left(Y + \frac{\epsilon_1 \beta^2}{\epsilon_{\max}} \right) \left[\ln Y - E_1(-Y) \right] \right\} \right\} dy$$

Choosing $C' = 0$ for the contour of integration and letting $iu = Y$, we obtain

$$f(X, \Delta) = \frac{\exp \left[\kappa \left(1 + \frac{\epsilon_1 \beta^2 \xi}{\epsilon_{\max}} \right) \right]}{2\pi \epsilon_1} \int_{-\infty}^{\infty} \exp \left\{ i\lambda u \right. \\ \left. - \kappa \left\{ e^{-iu} - \left(iu + \frac{\epsilon_1 \beta^2}{\epsilon_{\max}} \right) \left[\ln iu - E_1(-iu) \right] \right\} \right\} du$$

Since $e^{-iu} = \cos u - i \sin u$,

$$\ln i u = \begin{cases} \ln e^{i\pi/2} |u| = i\pi/2 + \ln |u| & u \geq 0 \\ \ln e^{-i\pi/2} |u| = -i\pi/2 + \ln |u| & u < 0 \end{cases}$$

and from Reference 13

$$E_1(-iu) = \begin{cases} C_1(|u|) - i S_1(u) + i\pi/2 & u \geq 0 \\ C_1(|u|) - i S_1(u) - i\pi/2 & u < 0 \end{cases}$$

$$f(X, \Delta) = \frac{\exp\left[\kappa\left(1 + \frac{\epsilon_1\beta^2\zeta}{\epsilon_{\max}}\right)\right]}{2\pi\epsilon_1} \int_{-\infty}^{\infty} \exp\left\{i\lambda u - \kappa\left\{\cos u - i \sin u - \left(iu + \frac{\epsilon_1\beta^2}{\epsilon_{\max}}\right)[\ln|u| - C_1(|u|) + i S_1(u)]\right\}\right\} du$$

where $C_1(u)$ is the cosine integral and $S_1(u)$ is the sine integral. Regrouping into real and imaginary parts

$$f(X, \Delta) = \frac{\exp\left[\kappa\left(1 + \frac{\epsilon_1\beta^2\zeta}{\epsilon_{\max}}\right)\right]}{2\pi\epsilon_1} \int_{-\infty}^{\infty} \exp\left\{\kappa\left\{\frac{\epsilon_1\beta^2}{\epsilon_{\max}} [\ln|u| - C_1(|u|)] - u S_1(u) - \cos u\right\} + i\lambda u + i\kappa\left\{u[\ln|u| - C_1(|u|)] + \frac{\epsilon_1\beta^2}{\epsilon_{\max}} S_1(u) + \sin u\right\}\right\} du$$

Letting

$$g_1(u) = \frac{\epsilon_1\beta^2}{\epsilon_{\max}} [\ln|u| - C_1(|u|)] - u S_1(u) - \cos u \quad (15)$$

and

$$g_2(u) = u [\ln|u| - C_1(|u|)] + \frac{\epsilon_1 \beta^2}{\epsilon_{\max}} S_1(u) + \sin u \quad (16)$$

and noting that $g_1(u)$ is an even function and $g_2(u)$ is an odd function, we get the distribution we shall call the "restricted energy loss distribution."

$$f(X, \Delta) = \frac{\exp \left[\kappa \left(1 + \frac{\epsilon_1 \beta^2 \xi}{\epsilon_{\max}} \right) \right]}{\pi \epsilon_1} \int_0^{\infty} e^{\kappa g_1(u)} \cos[\lambda u + \kappa g_2(u)] du \quad (17)$$

Comparing these results with the results of Vavilov's original derivation where

$$f(X, \Delta) = \frac{\exp[\kappa(1 + \beta^2 \xi)]}{\pi \epsilon_{\max}} \int_0^{\infty} e^{\kappa g_1(u)} \cos[\lambda u + \kappa g_2(u)] du$$

$$\kappa = \frac{X\xi}{\epsilon_{\max}}$$

$$\lambda = \frac{\Delta - \bar{\Delta}}{\epsilon_{\max}} - \kappa(\beta^2 + 1 - \xi)$$

$$g_1(u) = \beta^2 [\ln|u| - C_1(|u|)] - u S_1(u) - \cos u$$

and

$$g_2(u) = u [\ln|u| - C_1(|u|) + \beta^2 S_1(u)] + \sin u$$

we note that ϵ_{\max} has been replaced by ϵ_1 in κ, λ before the integral, and that λ has an additional logarithmic term. Also, β^2 has been replaced by $\epsilon_1 \beta^2 / \epsilon_{\max}$ in the exponential and in $g_1(u)$ and $g_2(u)$. Thus, simply replacing ϵ_{\max} by ϵ_1 in Vavilov's distribution will not give the correct distribution.

To evaluate the sine and cosine integrals which occur in equations (15) and (16), we use the following approximations:

$$C_1(u) = \begin{cases} \zeta + \ln u & u \leq 0.01 \\ \zeta + \ln u + \sum_{j=1}^{\infty} \frac{(-1)^j u^{2j}}{(2j)! 2j} & 0.01 < u < 1.0 \\ G(u) \sin u - H(u) \cos u & 1.0 \leq u < 50.0 \\ \frac{\sin u}{u} & u \geq 50.0 \end{cases} \quad (18)$$

$$S_1(u) = \begin{cases} u & u \leq 0.01 \\ \sum_{j=0}^{\infty} \frac{(-1)^j u^{2j+1}}{(2j+1)! (2j+1)} & 0.01 < u < 1.0 \\ \pi/2 - G(u) \cos u - H(u) \sin u & 1.0 \leq u < 50.0 \\ \pi/2 - \frac{\cos u}{u} & u \geq 50.0 \end{cases} \quad (19)$$

where

$$G(u) = \frac{1}{u} \frac{(u^8 + a_1 u^6 + a_2 u^4 + a_3 u^2 + a_4)}{(u^8 + a_5 u^6 + a_6 u^4 + a_7 u^2 + a_8)}$$

$$H(u) = \frac{1}{u^3} \frac{(u^8 + b_1 u^6 + b_2 u^4 + b_3 u^2 + b_4)}{(u^8 + b_5 u^6 + b_6 u^4 + b_7 u^2 + b_8)}$$

and

$$\begin{array}{ll} a_1 = 38.027264 & a_5 = 40.021433 \\ a_2 = 265.187033 & a_6 = 322.624911 \\ a_3 = 335.677320 & a_7 = 570.236280 \\ a_4 = 38.102495 & a_8 = 157.105423 \end{array}$$

$b_1 = 42.242855$	$b_5 = 48.196927$
$b_2 = 302.757865$	$b_6 = 482.485984$
$b_3 = 352.018498$	$b_7 = 1114.978885$
$b_4 = 21.821899$	$b_8 = 449.690326$

The series was terminated at the term which was 10^{-6} of the sum to that term.

Since most of the contribution in the integral in equation (17) is near the origin, the integration can be terminated at some finite limit. Simpson's rule was used to perform the numerical integration. Difficulties are encountered in obtaining good convergence of the integral where κ is small and on the tails of the distribution where $|\kappa|$ is large. Typically, for a κ of 0.87, good convergence was obtained on the tails [$f(X,\Delta) \approx 10^{-3}$] by integrating to a u of 20.0 with 6000 integration steps. At a κ of 19.3, integration to 1.5 with 2500 steps yielded good convergence. Good convergence here is taken as more than two significant figures since the test is applied at the extremes of distribution. Nearer the maximum of the distribution, convergence is much better than this. The test for good convergence was a second calculation where the upper bound of the integration was doubled and the number of integration steps was quadrupled.

B. Results for the Restricted Energy-Loss Distribution

In this section, we show some of the results obtained using the restricted energy-loss distribution derived above to calculate the energy-loss distribution due to low-energy transfers.

Taking the ionization chamber in Reference 1 as a typical example, we show (Fig. 1) the energy-loss distribution for an iron nucleus incident at 2.5 GeV/nucleon on a 5.1-cm-thick chamber containing 90-percent argon and 10-percent methane at 1 atmosphere. The curve for "no cutoff" is the regular Vavilov distribution which as usual is skewed to the right, peaking at an energy slightly below the mean energy loss $\bar{\Delta}$ of 9.16 MeV. The stopping power $S(E)$ used to calculate $\bar{\Delta}$ was the proton stopping power at the same energy per nucleon multiplied by Z^2 . The electron density weight average of the argon and the methane stopping power tabulated in Reference 14 were used to approximate the stopping power of the mixture. As would be expected, as the cutoff ϵ_1 is decreased, the tail to the right of the distribution maximum disappears, making the distribution more Gaussian and the mean of the distribution decrease.

III. HIGH-ENERGY DELTA-RAY DISTRIBUTION

In this section, we describe the number and energy distribution of the high-energy delta rays to be used and test its validity.

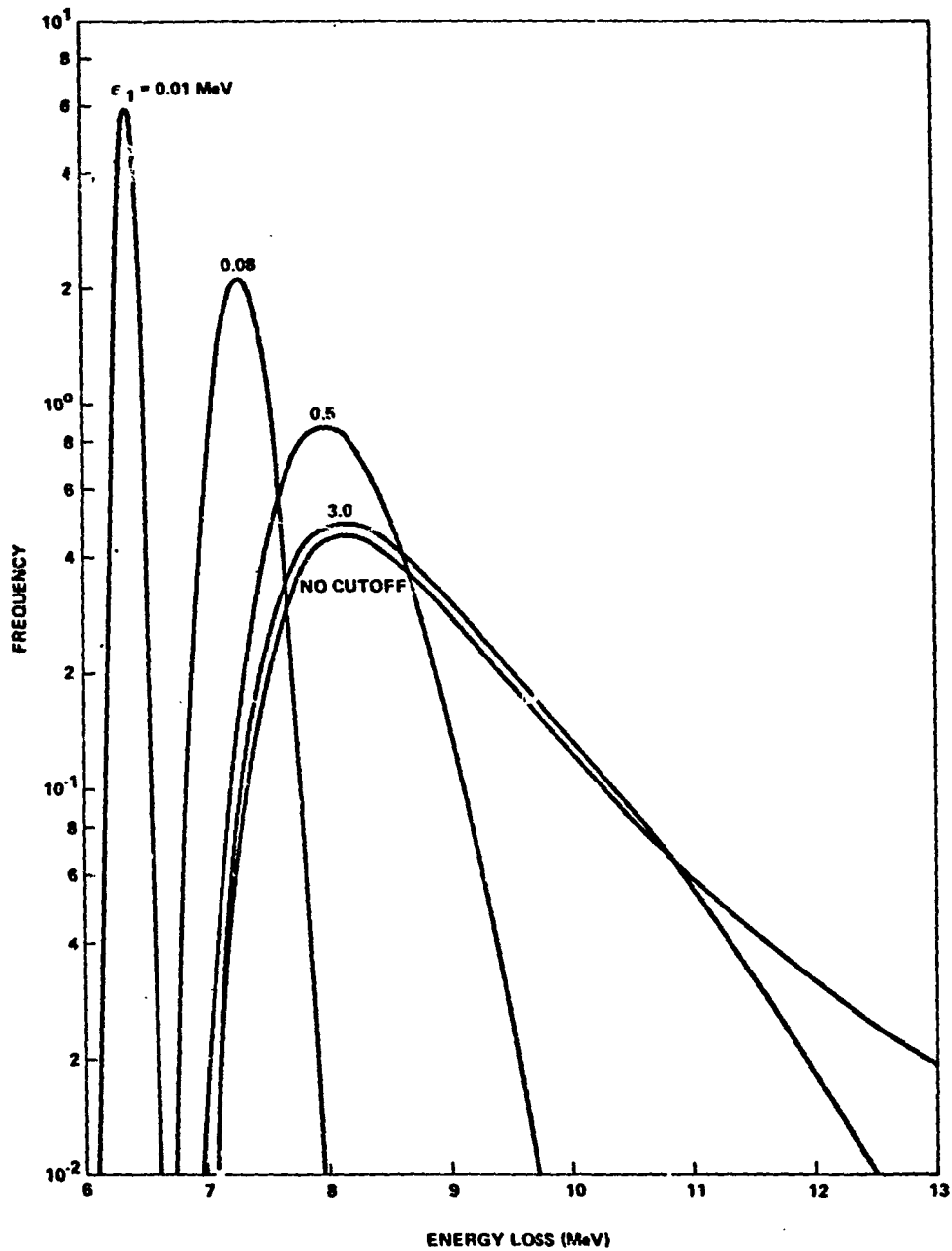


Figure 1. Restricted energy loss distribution with various delta-ray energy cutoffs for an iron nucleus (Fe^{56}) with an energy of 2.5 GeV/nucleon for a pathlength of 5.1 cm in a mixture of 90-percent argon and 10-percent methane at 1 atmosphere of pressure. ϵ_{max} was 12.853 MeV.

Because equation (11) applies above the cutoff energy ϵ_1 , the average number of delta rays produced along the pathlength X above ϵ_1 is given by

$$n_o = \int_{\epsilon_1}^{\epsilon_{\max}} \frac{X\xi}{\epsilon^2} \left(1 - \frac{\beta^2\epsilon}{\epsilon_{\max}} \right) d\epsilon$$

or

$$n_o = X\xi \left(\frac{1}{\epsilon_1} - \frac{1}{\epsilon_{\max}} + \frac{\beta^2}{\epsilon_{\max}} \ln \frac{\epsilon_1}{\epsilon_{\max}} \right) \quad (20)$$

Thus, the energy distribution of the high-energy delta rays is given by

$$n(\epsilon) = \frac{X\omega(E, \epsilon)}{n_o}$$

or

$$n(\epsilon) = \frac{\frac{1}{\epsilon^2} \left(1 - \frac{\beta^2\epsilon}{\epsilon_{\max}} \right)}{\frac{1}{\epsilon_1} - \frac{1}{\epsilon_{\max}} + \frac{\beta^2}{\epsilon_{\max}} \ln \frac{\epsilon_1}{\epsilon_{\max}}} \quad (21)$$

Since the production of a high-energy delta ray along the path of the primary particle path is a rather rare event, and since events of this type are independent of each other, we assume that the distribution of the number K of delta rays produced above ϵ_1 is Poisson, with a mean of n_o or

$$P(K) = \frac{n_o^K e^{-n_o}}{K!} \quad (22)$$

To test the assumption of equation (22), we performed a small Monte-Carlo calculation to determine the distribution of energy lost to high-energy delta rays by primary particles. For each of a set of primary particles, we sampled a number K from distribution $P(K)$ then we sampled K energies ϵ from $n(\epsilon)$ and summed them to obtain the energy loss of each primary particle. (See Appendix B for a description of sampling techniques.) Figure 2 shows the resulting distribution for 5000 iron nuclei incident on the argon-methane mixture, as in Figure 1. The cutoff energy ϵ_1 was 0.08 MeV.

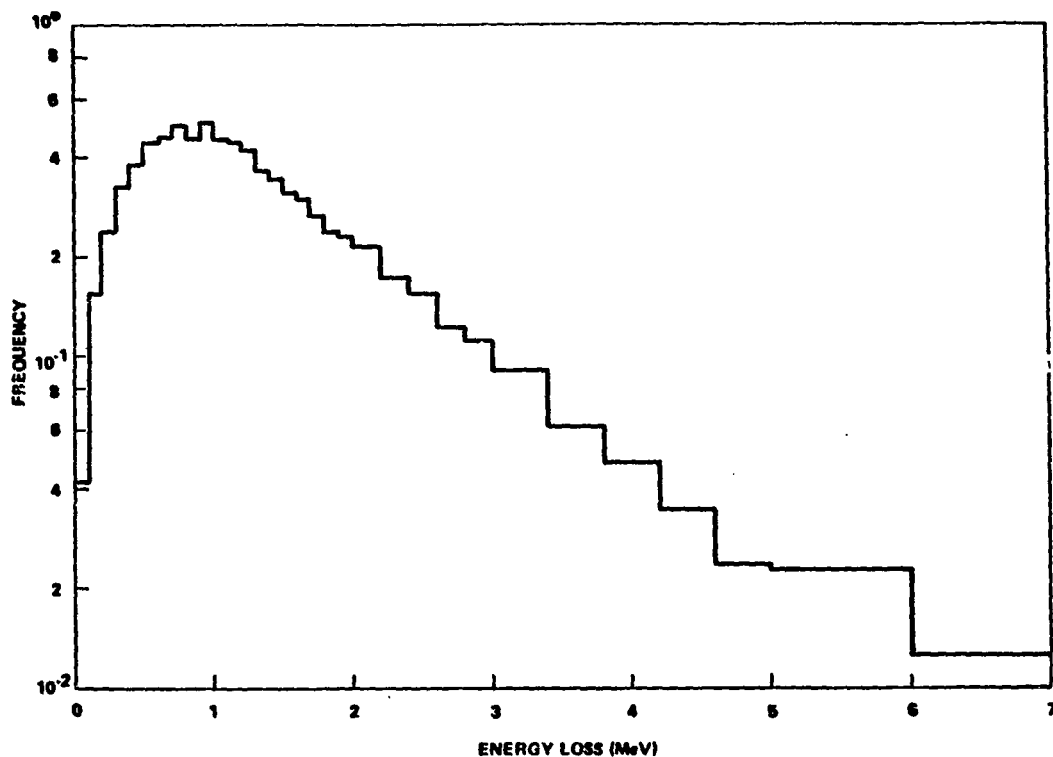


Figure 2. Energy loss distribution due to delta rays with energies above 0.80 MeV for an iron nucleus (Fe^{56}) with an energy of 2.5 GeV/nucleon for a pathlength of 5.1 cm in a mixture of 90-percent argon and 10-percent methane at 1 atmosphere of pressure.

The total energy loss is the sum of the energy lost to low-energy delta rays and the energy lost to high-energy delta rays. According to Reference 12, if a random variable Z is given by

$$Z = t + u \quad ,$$

then the frequency distribution of Z is given by the convolution integral

$$f_1(Z) = \int_{-\infty}^{\infty} f_2(Z - t) f_3(t) dt \quad (23)$$

where $f_2(u)$ is the frequency distribution of u and $f_3(t)$ is the frequency distribution of t . Since the distributions used here are zero over the negative range, the distribution of total energy loss $f_T(\Delta_T)$ is given by

$$f_T(\Delta_T) = \int_0^{\Delta_T} f(X, \Delta_T - t) f_{mc}(t) dt \quad (24)$$

where Δ_T is the total energy loss and $f_{mc}(t)$ is the distribution of loss caused by high-energy delta rays, determined by the Monte-Carlo calculation. Figure 3 shows the result of applying equation (24) to the distribution shown in Figure 2 and the corresponding distribution in Figure 1. The distribution shown in Figure 3 is practically identical to the distribution in Figure 1 where no cutoff is used except in the range between 12.0 and 13.0 MeV. (The discrepancies here are believed to be purely statistical in nature. The number of histories which gave contributions in this region was small.) Similar results have been obtained for other primary particle charges and energies and for different energy cutoffs ϵ_1 . Thus, we believe the assumption of equation (22) is valid.

IV. HIGH-ENERGY, DELTA-RAY TRANSPORT AND ENERGY DEPOSITION

In this section, we describe the method of transporting the high-energy delta rays produced in the ionization chamber and surrounding material and of calculating their energy deposition in the chamber gas.

Since the chamber consists of a number of materials and has a fairly complex geometry, Monte-Carlo transport techniques are the only ones that are easily applicable. A pure simulation, following the consequences of each individual scatter as is sometimes done with neutrons or gamma rays, is not used, because an electron interacts with so many atomic electrons in the process of slowing down. Instead, the electron path is divided into several segments, and a new direction of travel is selected from a multiple scattering distribution at the end of each segment. The scheme used here follows closely those described by Berger [16] and Perkins [17]. First, an energy grid is set up uniformly spaced in the logarithm of energy between ϵ_1 and ϵ_{max} ; i.e., each energy ϵ_i is larger than the preceding energy ϵ_{i-1} by a fixed percentage (usually about 5 percent). Second, using the

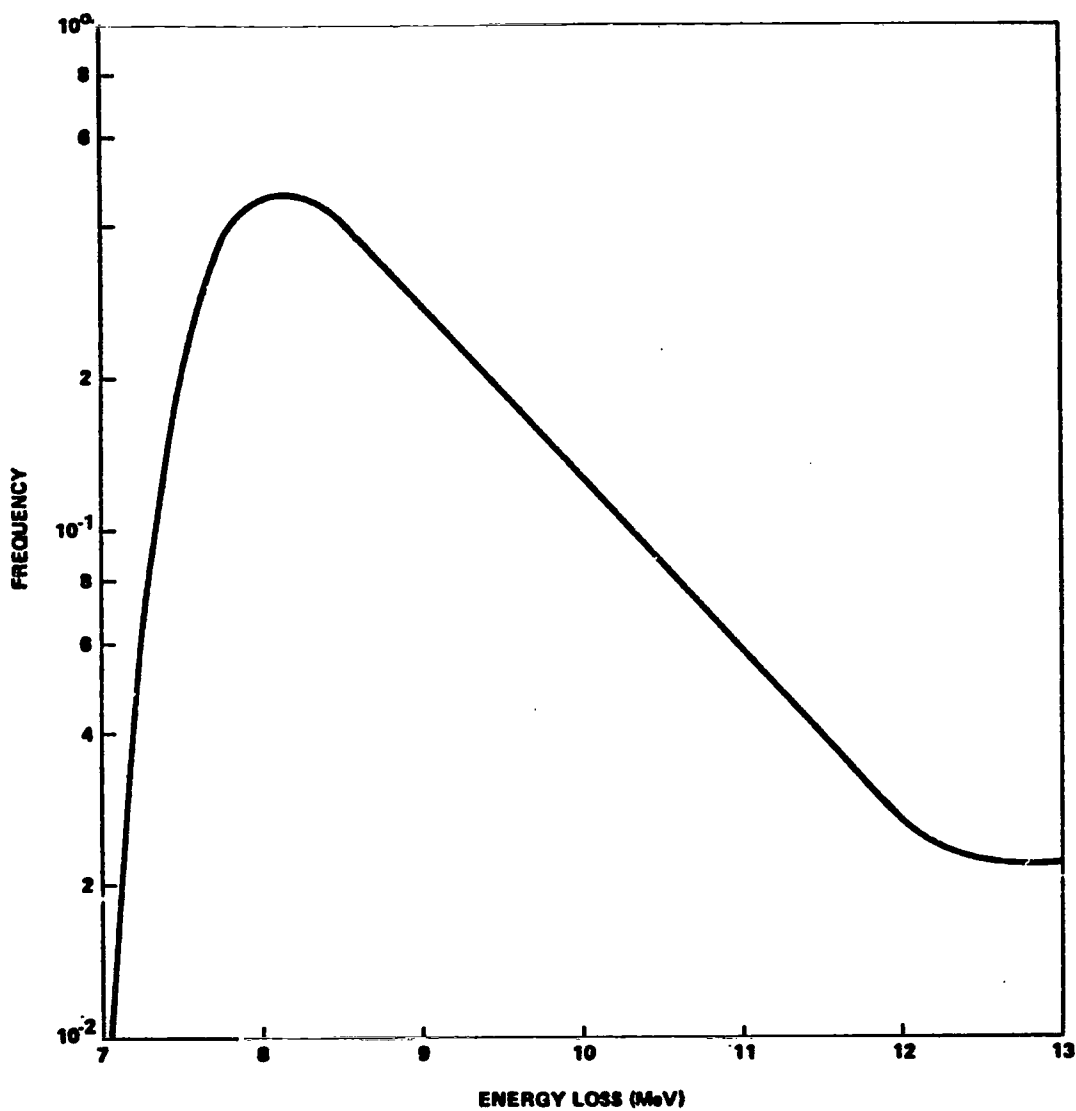


Figure 3. Total energy loss distribution calculated using the convolution integral [equation (24)] on the distribution shown in Figure 2 and the corresponding distribution ($\epsilon_1 = 0.08$ MeV) from Figure 1.

continuous-slowng-down approximation, the distance traveled ΔX_I in losing energy $\epsilon_I - \epsilon_{I-1}$ is determined from the total electron stopping power $S_T(\epsilon)$ [18] by

$$\Delta X_I = \frac{1}{\rho} \int_{\epsilon_{I-1}}^{\epsilon_I} \frac{d\epsilon}{S_T(\epsilon)} \quad (25)$$

where ρ is the material density. Since ϵ_I is near ϵ_{I-1} , equation (25) is approximated by

$$\Delta X_I \approx \frac{\ln \frac{\epsilon_I}{\epsilon_{I-1}}}{\rho \ln \frac{\epsilon_{I-1} S_T(\epsilon_I)}{\epsilon_I S_T(\epsilon_{I-1})}} \frac{\epsilon_{I-1}}{S_T(\epsilon_{I-1})} - \frac{\epsilon_I}{S_T(\epsilon_I)} \quad (26)$$

which assumes a power law connecting points $S_T(\epsilon_I)$ and $S_T(\epsilon_{I-1})$ on the stopping power curve. Where mixtures are involved, the stopping power is the average of the stopping powers of the elements or compounds in the mixture weighted by the corresponding electron densities. Third, given the energy lost and the distance traveled, the Moliere multiple scattering parameters (19, 20, 21) are calculated. (Appendix C describes the Moliere distribution.)

The Moliere distribution was selected over other distributions that are theoretically more accurate because it can be very rapidly sampled. (The comparisons in Figures 4, 5, and 6 show that the Moliere distribution is adequate for our purposes.) Since each primary particle can produce several hundred high-energy delta rays in passing through the ionization chamber and surrounding material, and since several thousand primary particles should be sampled to obtain satisfactory statistical accuracy, a multiple scattering distribution that can be rapidly evaluated is of prime importance in making the calculation possible.

An electron history proceeds as follows: The electron initial energy is sampled from equation (21) (see Appendix B) and the nearest grid energy ϵ_I is taken as the actual starting energy (Fig. 7). The electron's initial spatial coordinates are sampled randomly along the segment of the primary particle's path in a region of a single material; i.e., if 100 electrons are generated along a path segment through the chamber wall, their initial coordinates are distributed randomly along that segment. If five electrons are generated on the chamber segment, their initial coordinates are random along that segment. Energy deposition by the electron is determined by taking the difference between the two possible sources of energy, the production of the electron in the chamber gas or the scattering of the electron into the chamber gas, and the one possible energy-loss mechanism, the escape of

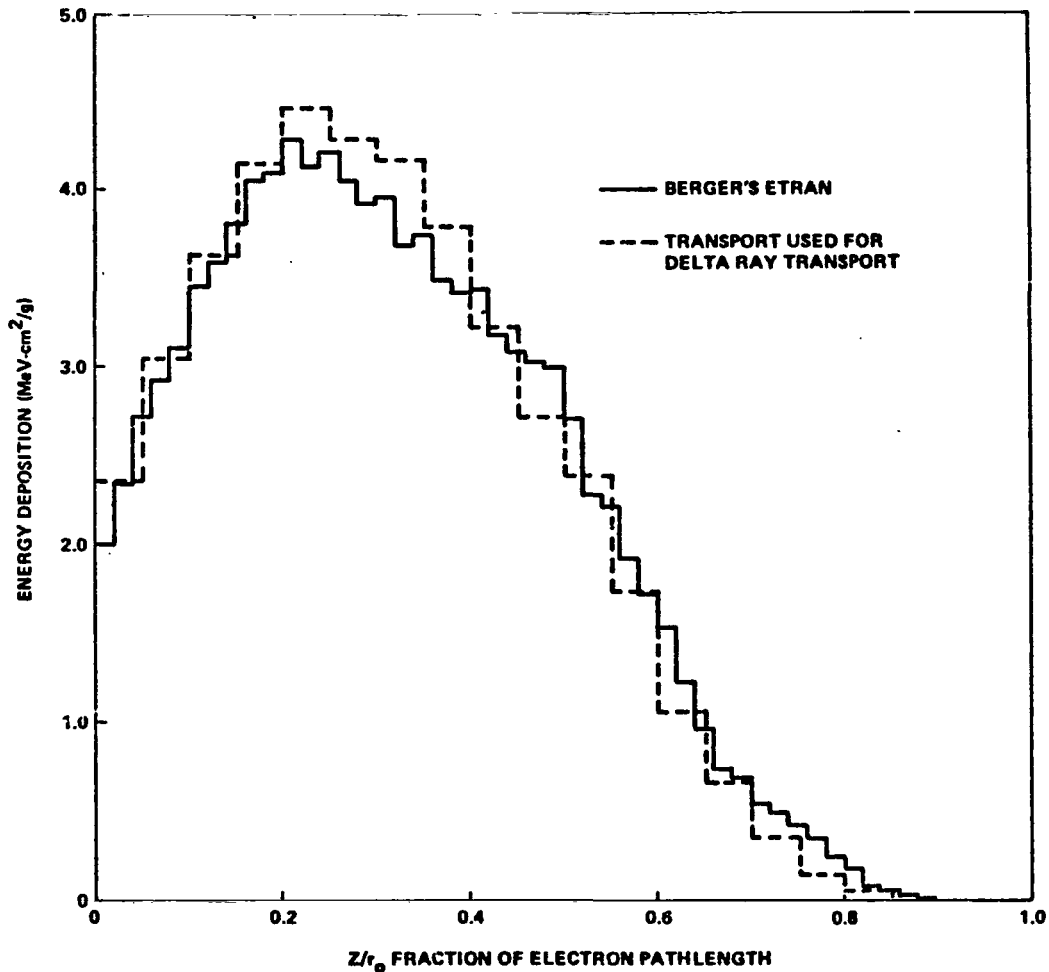


Figure 4. Energy deposition for 0.5 MeV electron normally incident on an aluminum slab.

the electron from the chamber gas. If the electron initial coordinates lie in the chamber gas, the initial energy is added to the sum of energy deposited by the electron in that chamber. Otherwise, the sum is set to zero. If the electron escapes from the chamber, the energy at escape will be subtracted from the sum. The angle between the initial electron direction and direction of the primary particle is calculated from

$$\cos \theta' = \frac{\left(1 + \frac{m}{M\gamma}\right)}{\beta} \sqrt{\frac{\epsilon_I}{\epsilon_I + 2mc^2}} \quad (27)$$

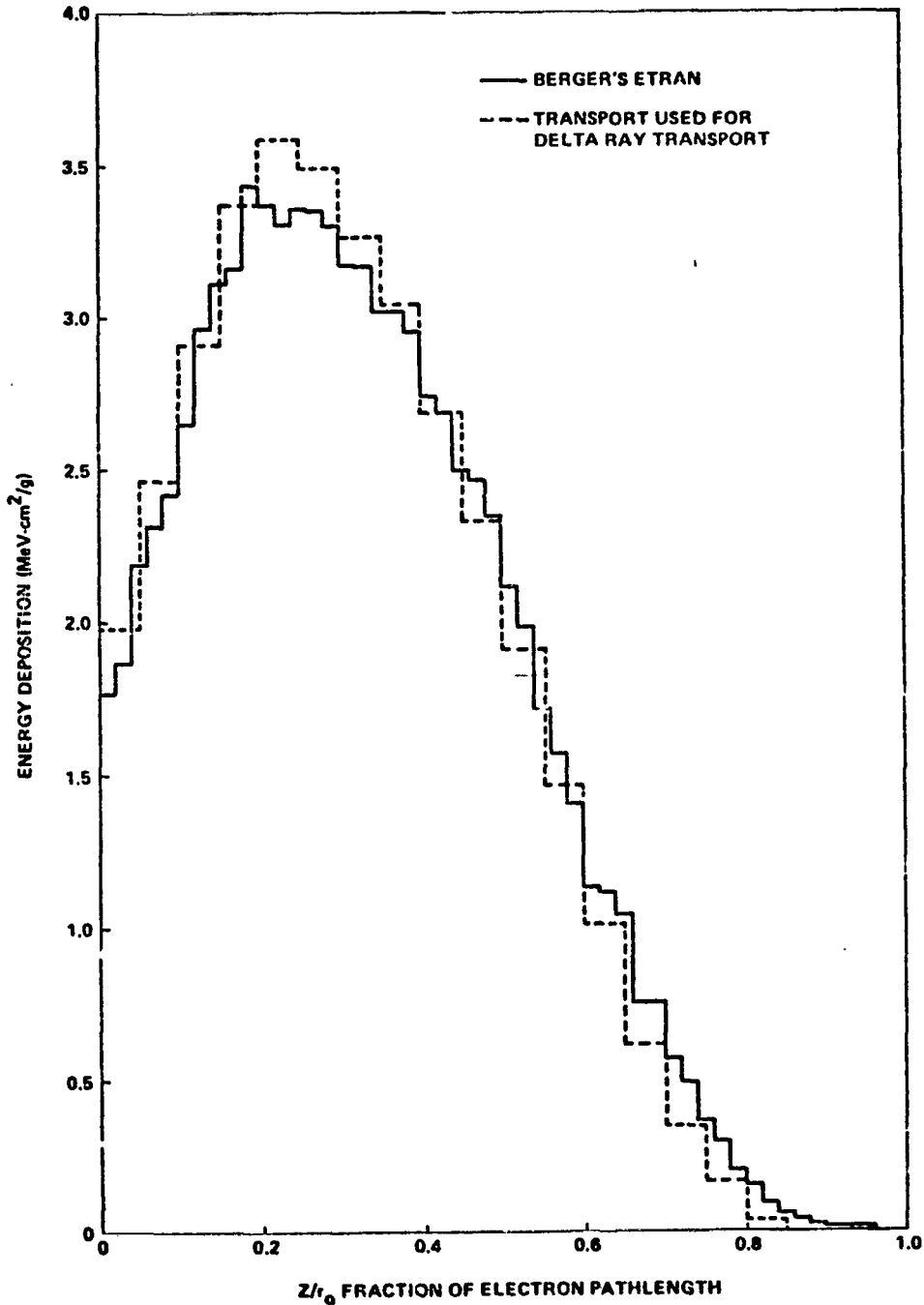


Figure 5. Energy deposition for 1.0 MeV electron normally incident on an aluminum slab.

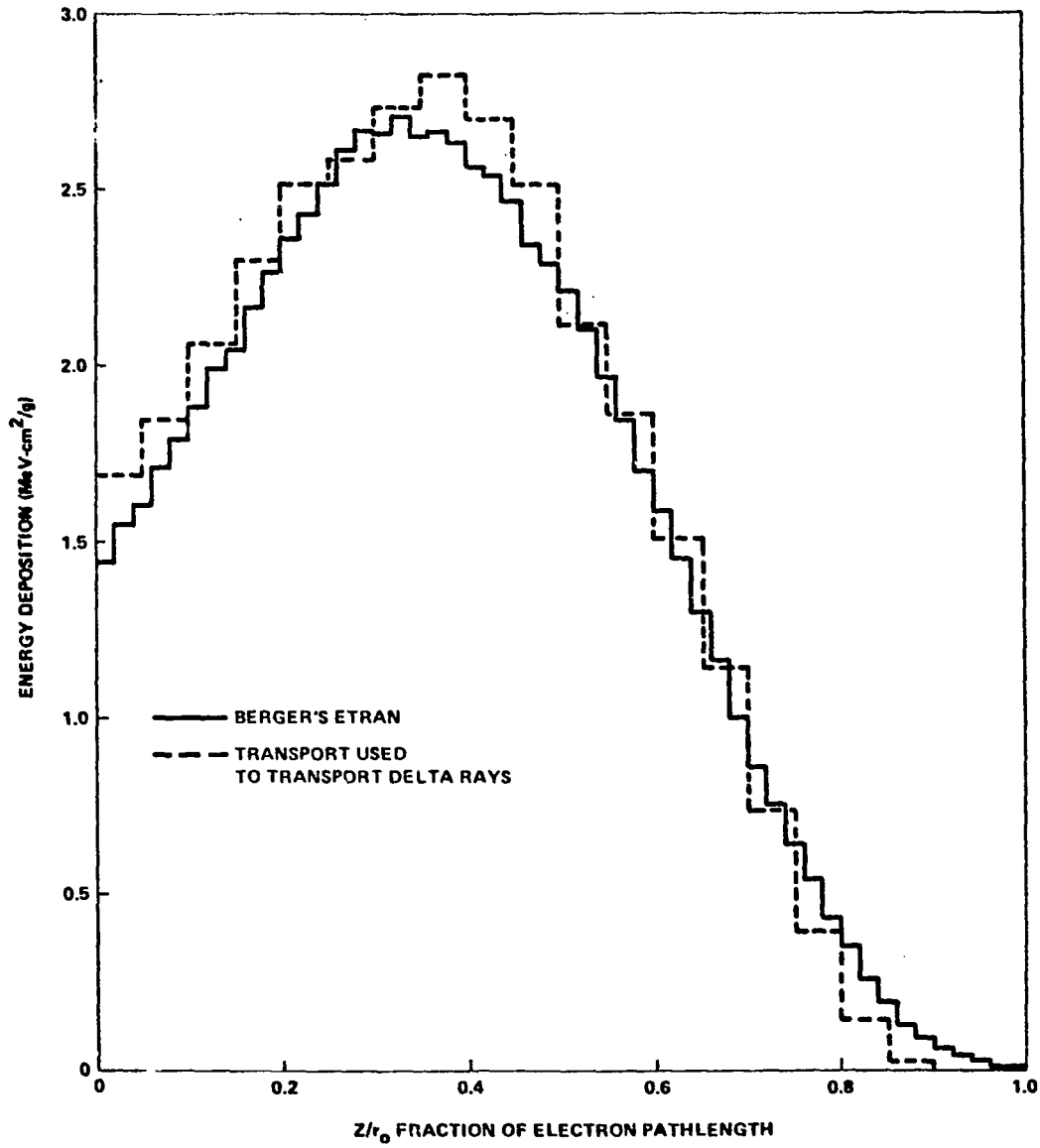


Figure 6. Energy deposition for 4.0 MeV electrons normally incident on an aluminum slab.

[see Appendix A for a derivation of equation (27)]; the direction cosines of the initial electron trajectory are calculated using the cosines of the primary particle path (see Appendix D). Then, the coordinates of the end of the first path segment are determined. Tests are made to determine if the chamber boundary has been crossed. If the electron has escaped from the chamber gas, the energy at the boundary determined by linear interpolation is subtracted from the energy sum deposited by the electron in that chamber. If the electron has scattered into the chamber gas, then the energy at the boundary is added to that chamber sum. When any chamber boundary is crossed, a new set of segment end coordinates must be calculated because of changes in density or stopping power. Then, tests are made for succeeding boundary crossings until the region is reached where the segment actually ends. A new direction is then sampled from the Moliere multiple scattering distribution, and the process of boundary testing starts over along the new path segment. The electron is followed in this fashion until it either escapes from the instrument or reaches ϵ_1 . At ϵ_1 , one last segment is taken whose length is the mean electron pathlength [18] at ϵ_1 .

As a check on the accuracy of the electron transport, calculations of energy deposition in a plane aluminum slab were made using the described method. Reference 22 describes similar calculations using Berger's program, ETRAN [16], which is recognized as one of the best electron transport codes presently available. Figures 4, 5, and 6 show comparisons of the results from Berger's program [22] and the transport described here for monoenergetic electrons normally incident on the slab surface at 0.5, 1.0, and 4.0 MeV, respectively. The energy grid separation was 5.0 percent, and the cutoff energy ϵ_1 was 0.08 MeV in our case. Results from our program tend to peak slightly higher in energy and drop more rapidly with energy. The differences are small and should not significantly affect the results of our calculations.

V. TOTAL ENERGY DEPOSITION

In this section, we show how the total energy deposition distribution for primary particles is calculated using the results of the previous sections.

In these calculations, the primary cosmic rays are presumed to arrive as a monoenergetic, monodirectional beam of a single isotope and to travel in a straight line through the instrument. Given the exterior point of incidence and the beam direction cosines, the pathlength in each chamber is determined and the low-energy, delta-ray energy deposition (restricted energy loss) distributions are calculated according to equation (17) for each chamber.

To obtain the high-energy, delta-energy distribution, we use Monte-Carlo techniques in one of two schemes, depending on the number of delta rays produced by the primary. If each primary on the average generates only a few (≤ 100) delta rays above the cutoff energy, a new set of electron histories can be generated for each primary particle as the primary is followed through the instrument. (The number and energy sampling is as described in Section III.) In most cases of interest, however, each primary produces on the order of 1000 high-energy electrons, and generating a new set of electrons for each primary particle becomes prohibitively expensive in terms of computer time. Instead, a set of

electrons is sampled from a table of electron histories previously generated and placed on magnetic tape, and the same electron history can be used several times. This approximation is valid if the table can contain a representative population of electrons. For the calculations shown here, 20 000 electron histories were generated in each region of the geometry that was crossed by the primary beam.

The electrons sampled for each primary particle are treated as follows: The initial energies of electrons that happen to be generated in a given chamber are summed and added to an energy loss/deposition for low-energy transfers sampled from the distribution given by equation (17) to obtain a total energy loss for the particle in the chamber. Next, the energy deposited in a given chamber by all electrons sampled for a primary is summed to obtain the energy deposited by high-energy electrons in the chamber. Combining this energy with the sampled low-energy electron loss/deposition sample yields the total energy deposited by the chamber primary. After several thousand primary particles have been sampled, the resulting energy losses and energy depositions are sorted into energy bins to give histograms approximating the frequency distributions for low-energy loss/deposition, high-energy deposition, total energy deposition, and total energy loss.

A second and better method for calculating the total deposition distribution — because it eliminates the statistical fluctuation of sampling from the low-energy loss/deposition distribution — is to use equation (23) in a convolution of the restricted energy-loss distribution from equation (17) and the histogram frequency distribution for high-energy electron energy deposition resulting from the Monte-Carlo calculation. This is the method that is used for the results that follow.

VI. RESULTS AND CONCLUSIONS

Figures 8 and 9 show the total energy deposition distribution calculated by the pure Monte-Carlo (the histogram) and the Monte-Carlo convolution (the smooth curve) for iron nuclei Fe^{56} normally incident at 2.5 GeV/nucleon on the double ionization chamber of Israel et al. [1]. The instrument was simulated by a stack of five rectangular slabs 99-cm long by 99-cm wide. The front slab which represents material between the primary beam and the first chamber plus the front chamber wall is 0.40 cm or 1.1 g/cm^2 of aluminum thick. The second slab which represents the first chamber gas is 5.1-cm thick. The gas is a mixture of 90-percent argon plus 10-percent methane at 1 atmosphere with a density of $1.6767 \times 10^{-3} \text{ g/cm}^3$. Thus, $8.5 \times 10^{-3} \text{ g/cm}^2$ of chamber gas is encountered by the beam. (The gas slab is identical to the one used for Figure 1.) The third slab representing the back wall of the front chamber plus the front wall of the back chamber is $6.0 \times 10^{-2} \text{ cm}$ or $1.6 \times 10^{-1} \text{ g/cm}^2$ of aluminum thick. The fourth slab is the gas of the second chamber and is identical to the second slab. The fifth slab is the back wall of the back chamber which is $3.0 \times 10^{-2} \text{ cm}$ or $8.0 \times 10^{-2} \text{ g/cm}^2$ of aluminum thick. We assumed that little energy is deposited in the chamber by electrons reflected from the side walls of the chamber or from material behind the back chamber wall so that electrons that entered these regions are allowed to escape from the geometry. The cutoff energy ϵ_1 was chosen to be 0.08 MeV so that comparisons can be made with curves in Figures 1, 2, and 3.

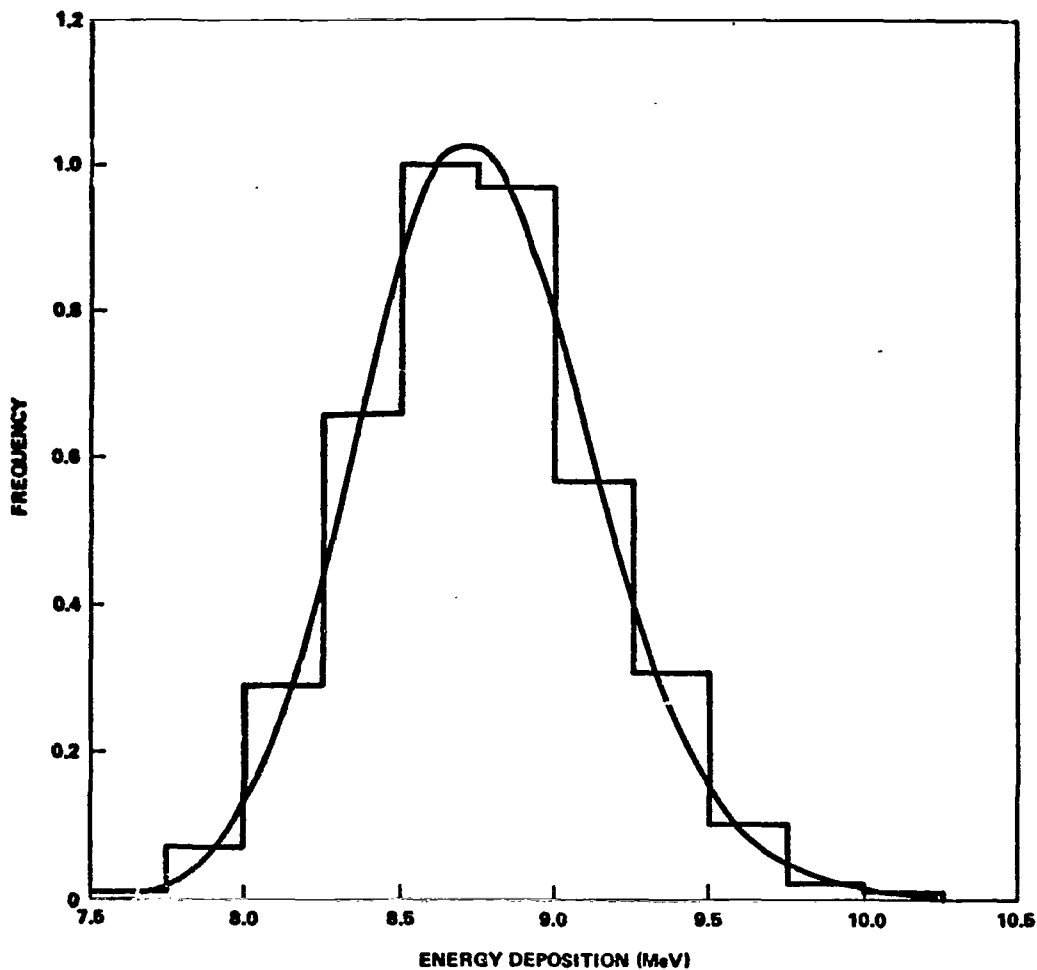


Figure 8. Calculated frequency distribution of energy deposition in the first of two stacked ionization counters of Israel et al. [1] by iron nuclei (Fe^{56}) normally incident at 2.5 GeV/nucleon. (The histogram is the pure Monte-Carlo calculation and the curve is the Monte-Carlo convolution.)

The distributions of Figures 8 and 9 appear to be Gaussian with no Landau tail present. The full width at half maximum is 0.9 MeV or about 10 percent of the mean energy deposition. The mean energy deposition is below the mean energy loss by about 3 percent, implying that energy deposition is not in equilibrium with energy loss. More energy is being transported out the back wall of the chamber than is being transported in the front wall, in agreement with Reference 23 which suggests that perhaps 6 g/cm² or more of material is required to reach equilibrium between the production and absorption of knock-on electrons. The most striking observation is the reduction of the full width at half maximum by a factor of two as compared with the width of the energy-loss distribution (Fig. 1).

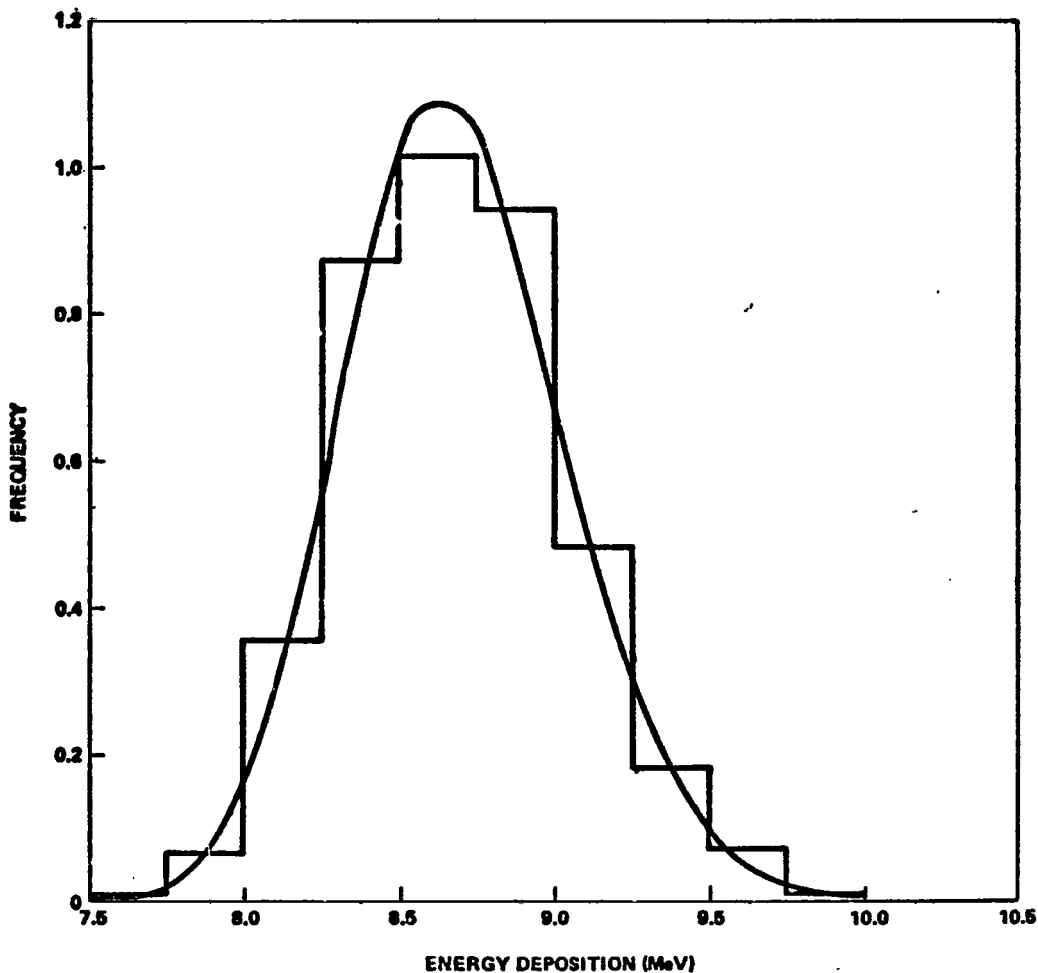


Figure 9. Calculated frequency distribution of energy deposition in the second of two stacked ionization counters of Israel, et al. [1] by iron nuclei (Fe^{56}) normally incident at 2.5 GeV/nucleon. The histogram is the pure Monte-Carlo calculation and the curve is the Monte-Carlo convolution.)

Observations by Israel et al. [1] on balloon flights from Palestine, Texas (where the geomagnetic cutoff is 4.5 MV), using the instrument simulated for Figures 8 and 9, indicate a width of 14 to 16 percent for the iron peak. (Their results are shown as the histograms in Figure 10 taken from Reference 1.) The measurements had several sources of fluctuations not considered here. Amplifier noise was Gaussian with σ_N equal to 2.2 percent of the mean pulse height due to normally incident relativistic iron. Uncertainties in the trajectory measurement were characterized by a σ_L of 2.1 percent. The experimenters also suggested

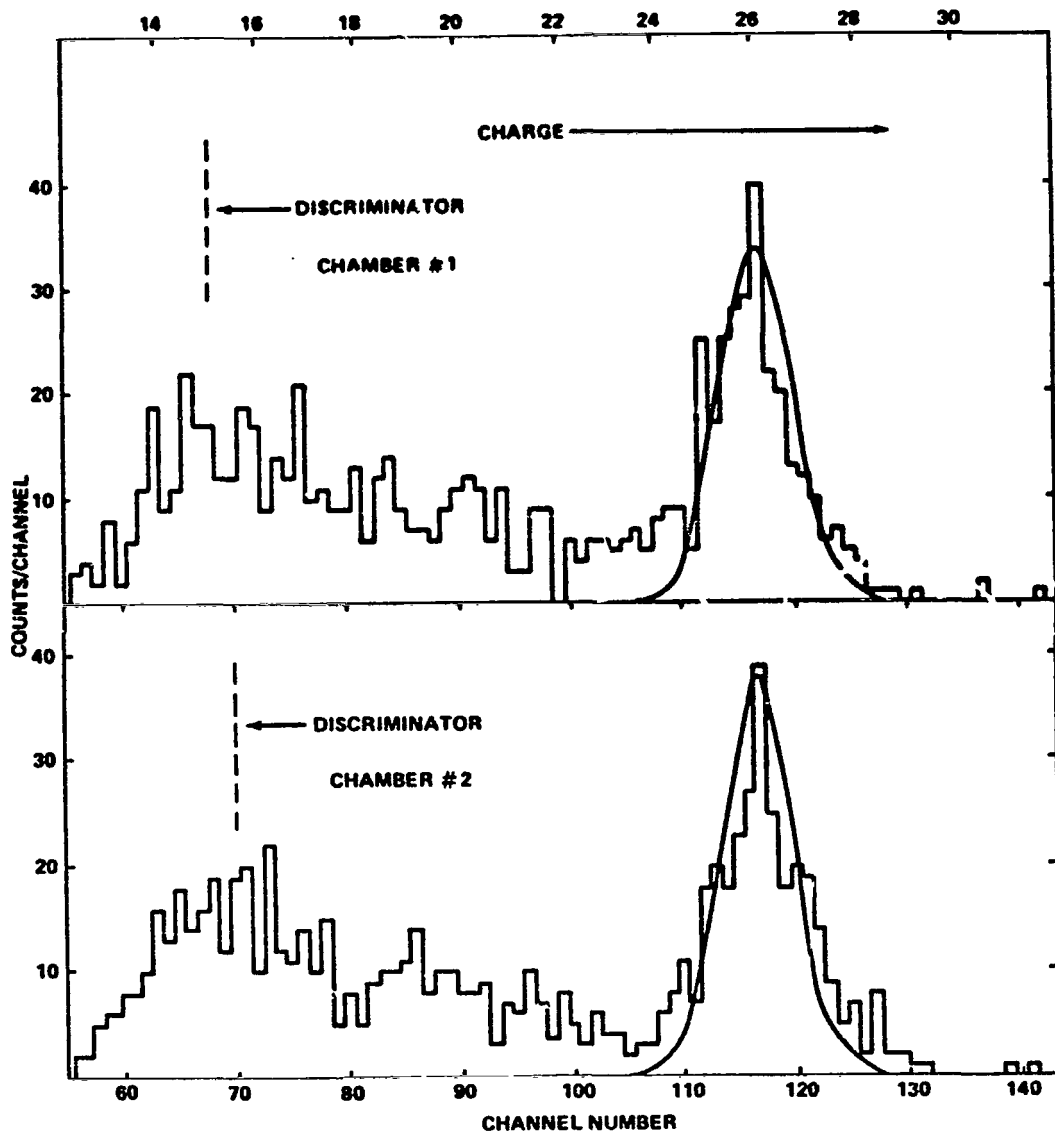


Figure 10. Comparison of Israel et al. [1] results with our calculated distribution including noise and contribution from charges 25 and 27.

that part of the width of the peak was because perhaps as many as 10 percent of the counts included under the peak were for charges of 25 and 27. The superimposed curves in Figure 10 are out-results with the other sources of fluctuations folded into our calculated distribution and with a contribution of 10 percent equally divided between charges 25 and 27. The curve is normalized to the total number of counts in channels 110 to 130, and energy deposition is assumed to be proportional to charge squared. The peak width with the other sources of fluctuation included is 13 percent of the mean energy deposition which is in reasonable agreement with their results.

Figure 11 demonstrates the importance of the surrounding material for the energy deposition calculation and shows the energy deposition distribution for the bare 5.1 gas slab used for the previous figures with no surrounding material. The peak energy has decreased by more than 1.0 MeV and the full width at half maximum is nearly halved compared with the complete geometry. Note that the distribution is merely shifted slightly from the corresponding energy loss/deposition distribution for ϵ_1 equal to 0.08 MeV in Figure 1 implying that high-energy electrons from material above the chamber contribute more to energy deposition in the chamber than do those high-energy electrons created in the chamber.

Figures 12 through 23 show the results of a study of the response as a function of charge of a proposed ionization chamber to be flown on a satellite [24]. The instrument actually consists of four chambers with the responses of the first and second chambers combined to obtain a single measurement of energy deposition. The third and fourth chambers were similarly coupled. In the calculations, the instrument was simulated by a stack of 50- by 50-cm rectangular slabs. The first slab representing material in front of the instrument was 0.37 cm or 1.0 g/cm² of aluminum. Next, there were eight alternating slabs 0.0508-cm or 0.4-g/cm² thick of iron representing the chamber walls and 3.0-cm thick representing gas. Last, there was the back wall of the last chamber which was like the other iron slabs. The gas was a mixture of 98-percent xenon and 2-percent carbon dioxide at 1 atmosphere. Thus, the gas slabs were 1.73 x 10⁻² g/cm² thick. The cosmic rays were taken as normally incident at the center of the front aluminum slab with an energy of 10.0 GeV/nucleon.

For lower charges (Figs. 12 through 15), we note that the Landau tail is still in evidence but that the distributions are not as skewed as the Vavilov energy-loss distribution would be. The variation of the distribution maximum with charge can be well represented as being proportional to charge squared, and the variation of the distribution width seems to be proportional to charge. The width again is much smaller for the energy deposition distribution than it would be for the energy-loss distribution.

In conclusion, the relationship between energy loss and energy deposited by primary cosmic rays is not simple. To determine the energy deposited in a small region, as is required for the analysis of data on heavy cosmic rays from ionization chambers and in other applications such as microdosimetry, the energy transport and deposition by high-energy secondary electrons must be considered. In the case of ionization chambers, the calculations described here show that the energy deposition frequency distribution is considerably narrower than the energy-loss distribution with the most probable energy deposition somewhat below the mean energy loss for the geometries considered. The deposition

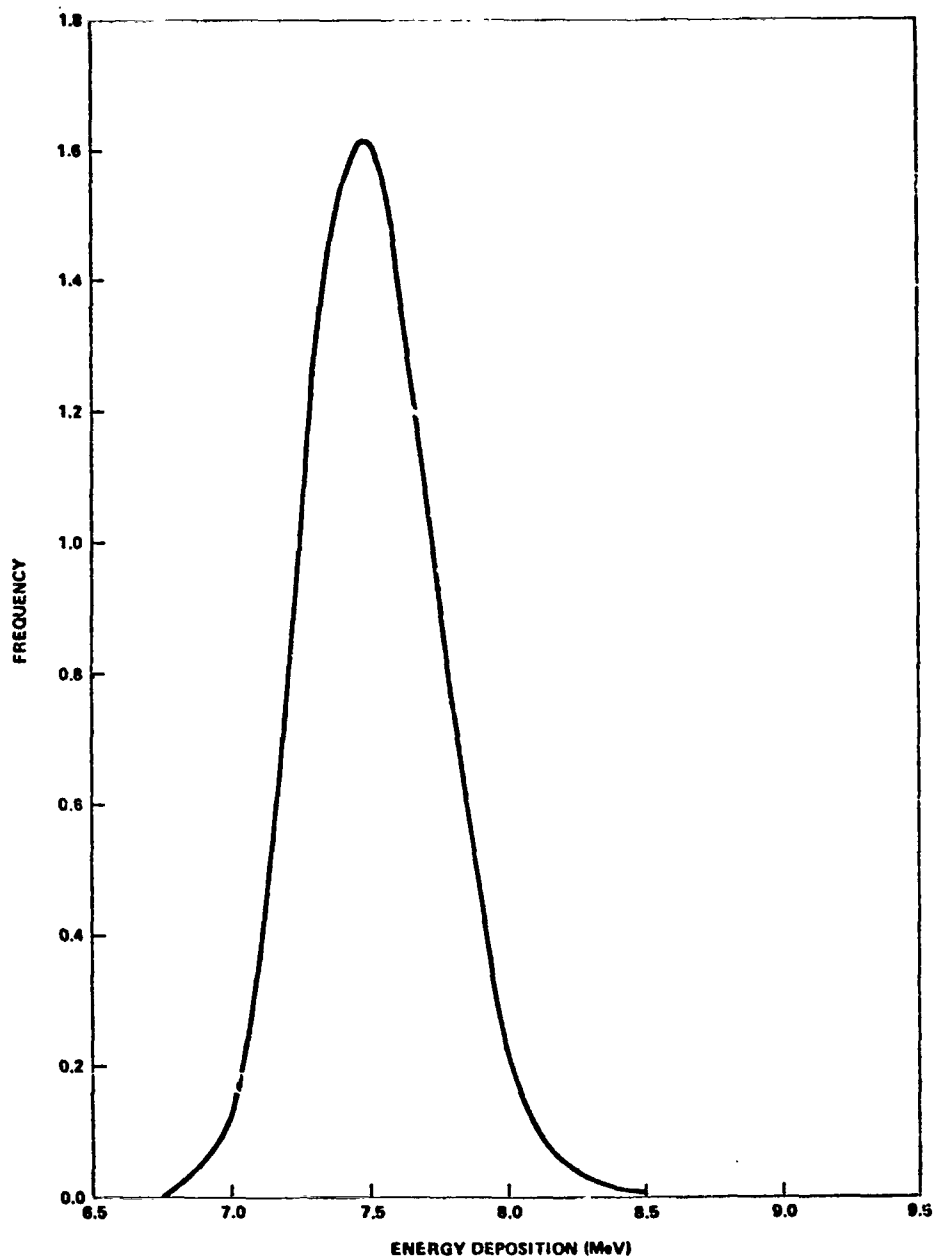


Figure 11. The energy deposition frequency distribution for iron (Fe^{56}) nuclei normally incident at 2.5 GeV/nucleon on a bare slab with dimensions $99 \times 99 \times 5.1$ cm composed of 90-percent argon and 10-percent methane at a pressure of 1 atmosphere.

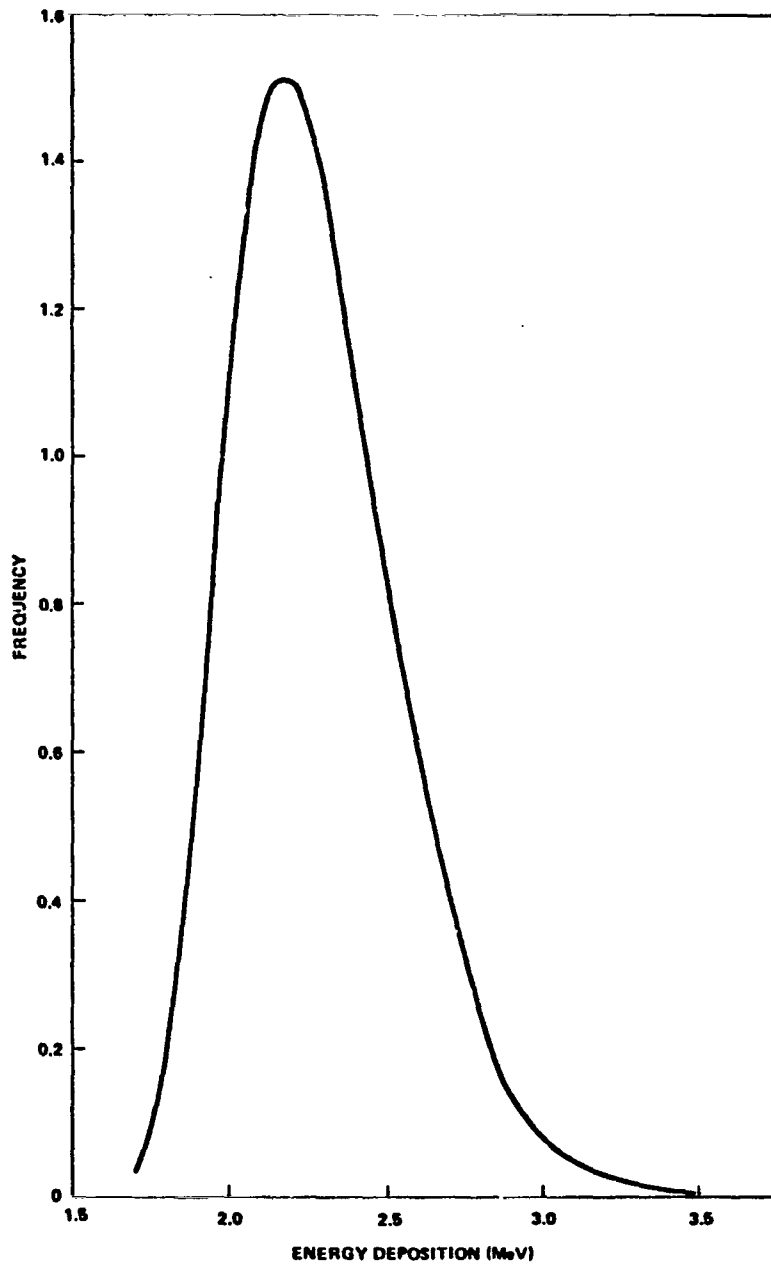


Figure 12. The energy deposition frequency distribution for nitrogen (N^{14}) nuclei normally incident at 10.0 GeV/nucleon on the four-chamber instrument. (These results are for the first two-chamber-coupled detector.)

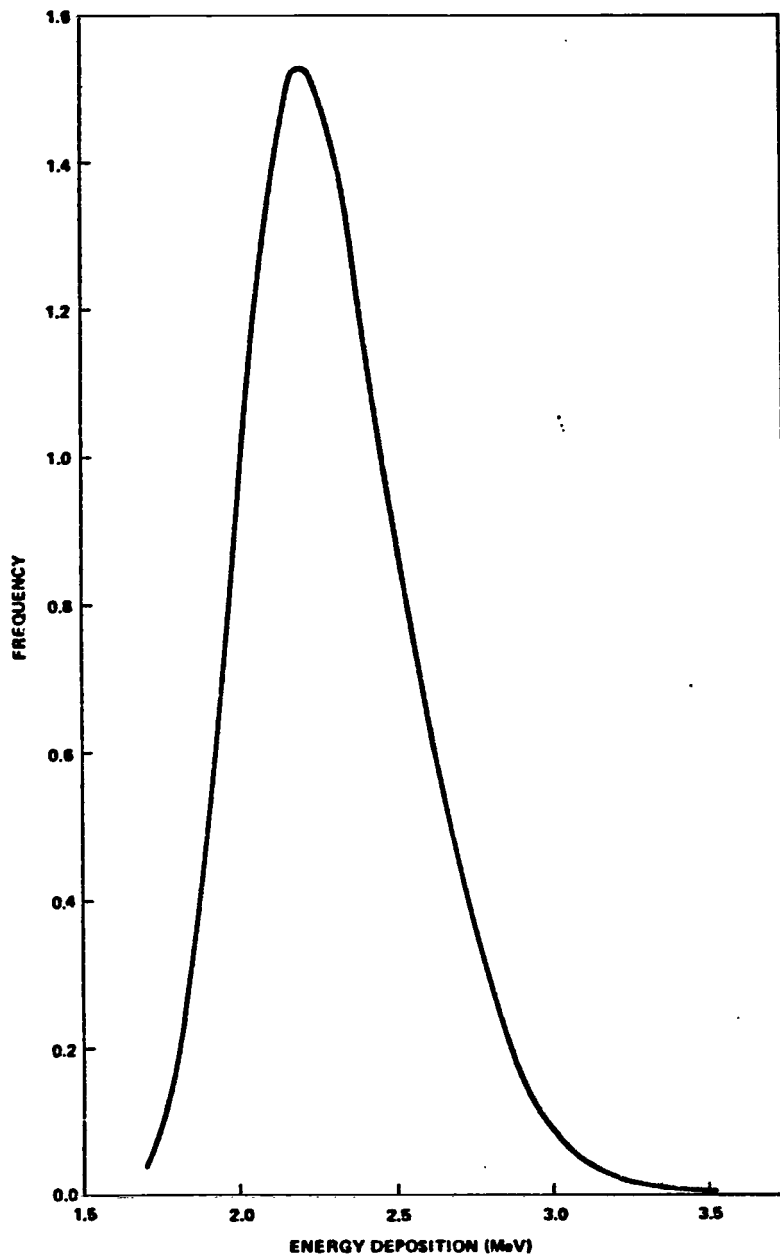


Figure 13. The energy deposition frequency distribution for nitrogen (N^{14}) nuclei normally incident at 10.0 GeV/nucleon on the four-chamber instrument. (These results are for the second two-chamber-coupled detector.)

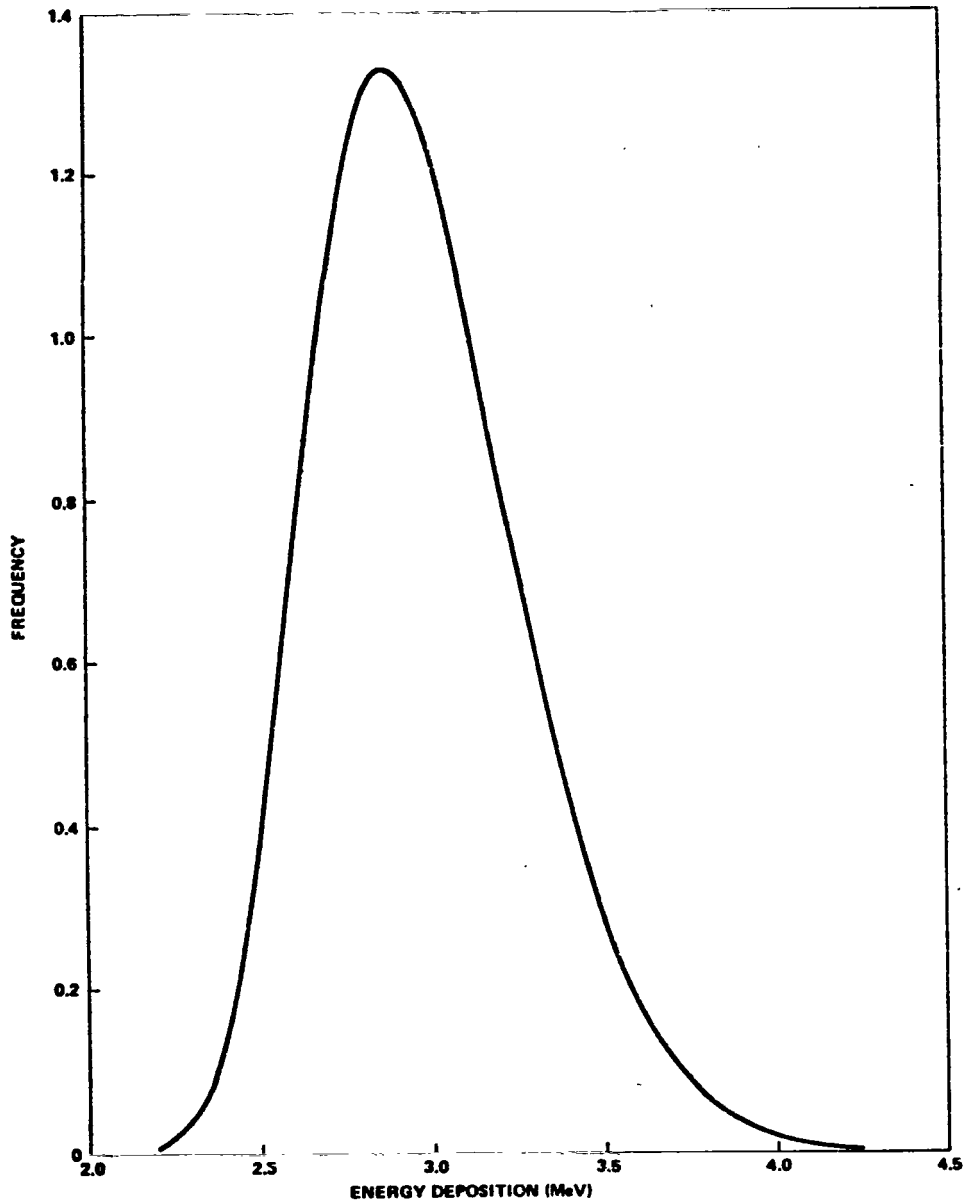


Figure 14. The energy deposition frequency distribution for oxygen (O^{16}) nuclei normally incident at 10.0 GeV/nucleon on the four-chamber instrument. (These results are for the first two-chamber-coupled detector.)

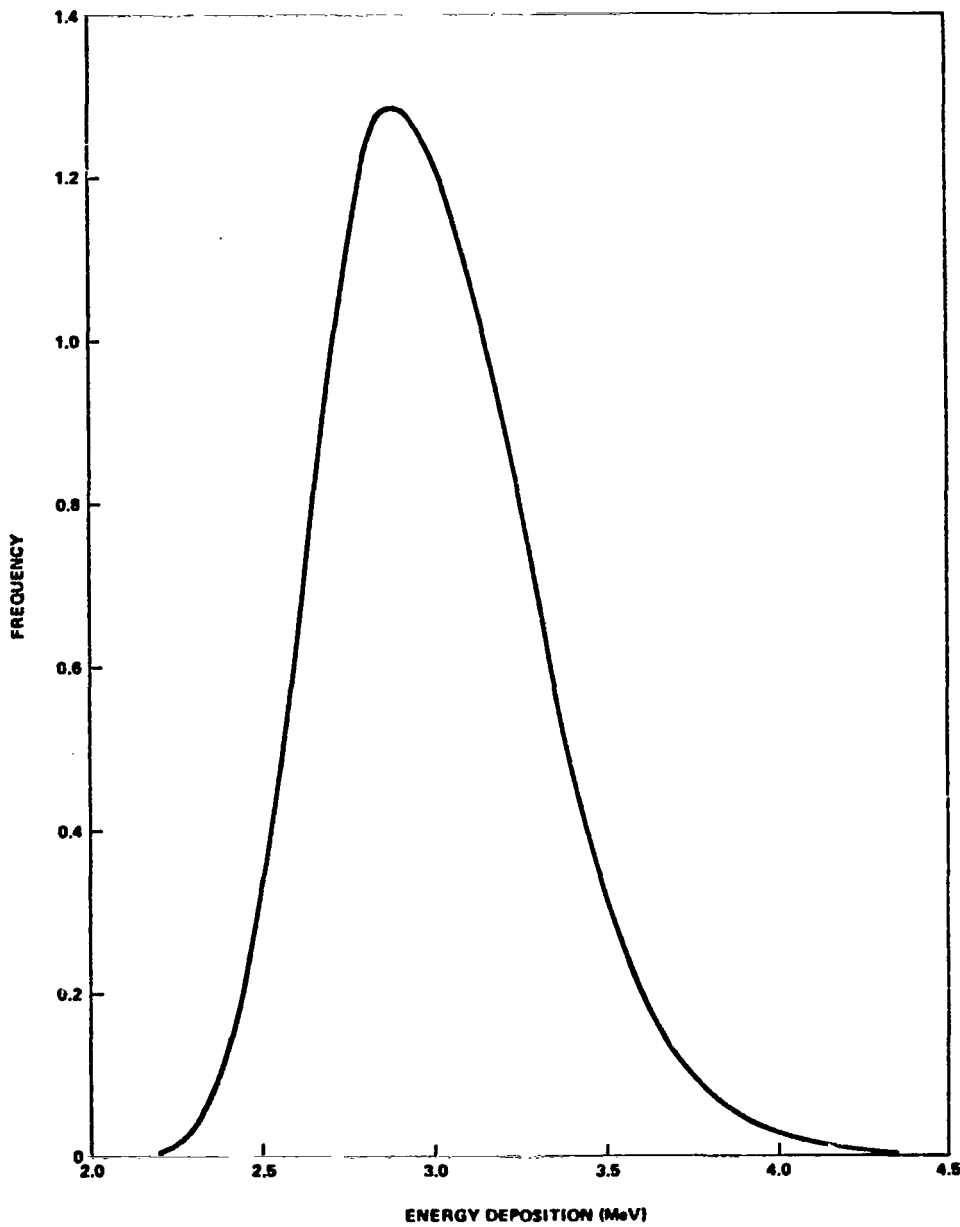


Figure 15. The energy deposition frequency distribution for oxygen (O^{16}) nuclei normally incident at 10.0 GeV/nucleon on the four-chamber instrument. (These results are for the second two-chamber-coupled detector.)

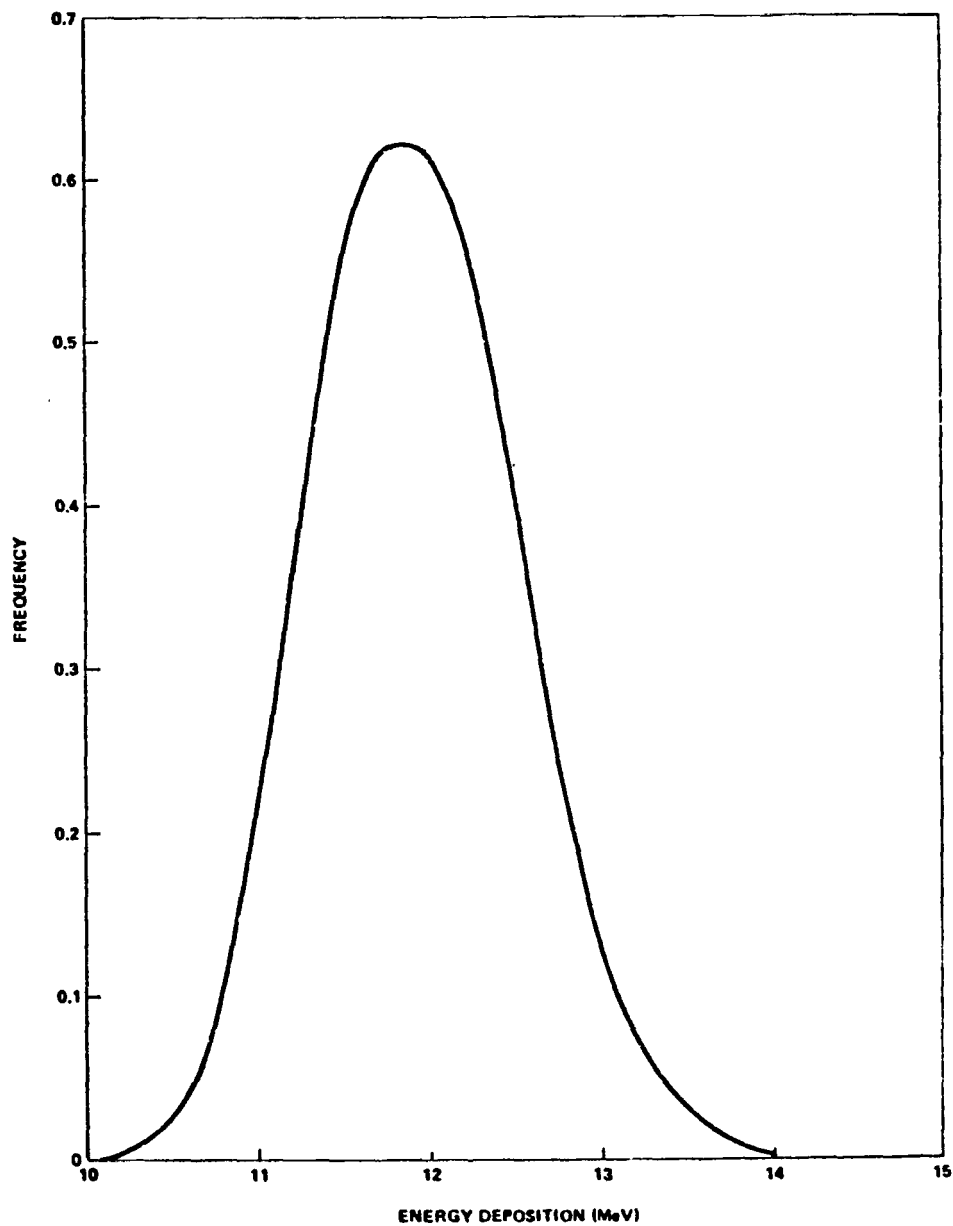


Figure 16. The energy deposition frequency distribution for sulfur (S^{32}) nuclei normally incident at 10.0 GeV/nucleon on the four-chamber instrument. (These results are for the first two-chamber-coupled detector.)

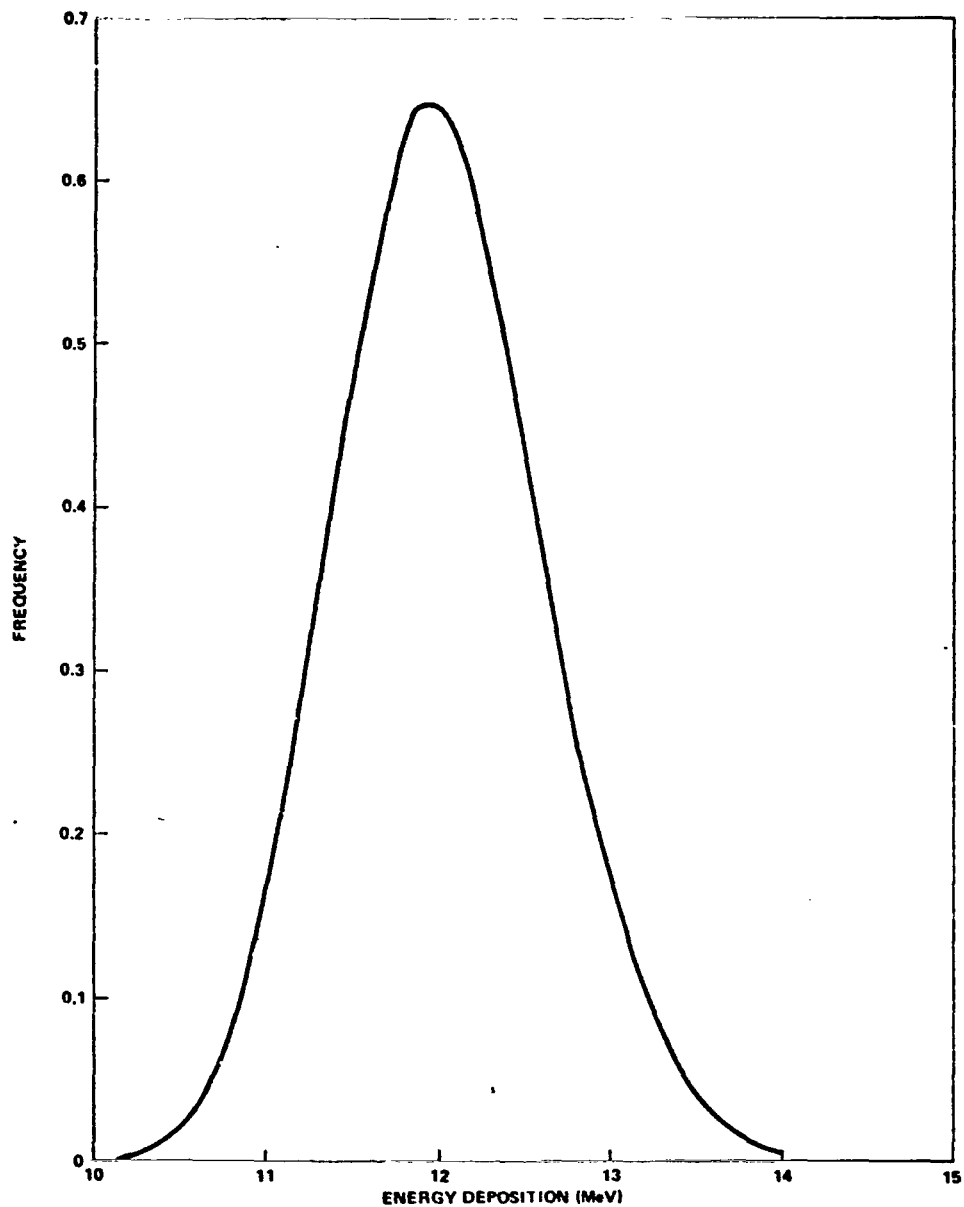


Figure 17. The energy deposition frequency distribution for sulfur (S^{32}) nuclei normally incident at 10.0 GeV/nucleon on the four-chamber instrument. (These results are for the second two-chamber-coupled detector.)

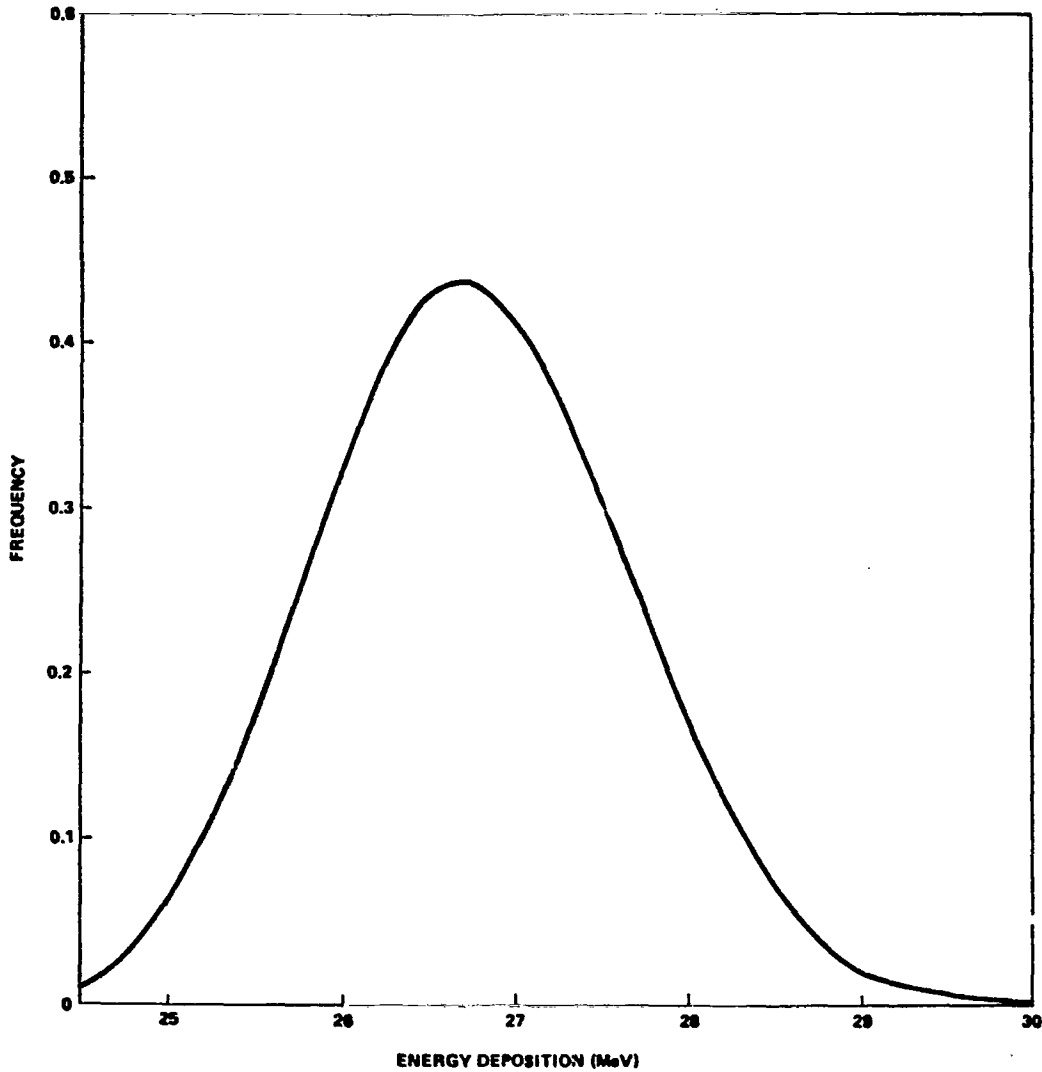


Figure 18. The energy deposition frequency distribution for chromium (Cr^{52}) nuclei normally incident at 10.0 GeV/nucleon on the four-chamber instrument. (These results are for the first two-chamber-coupled detector.)

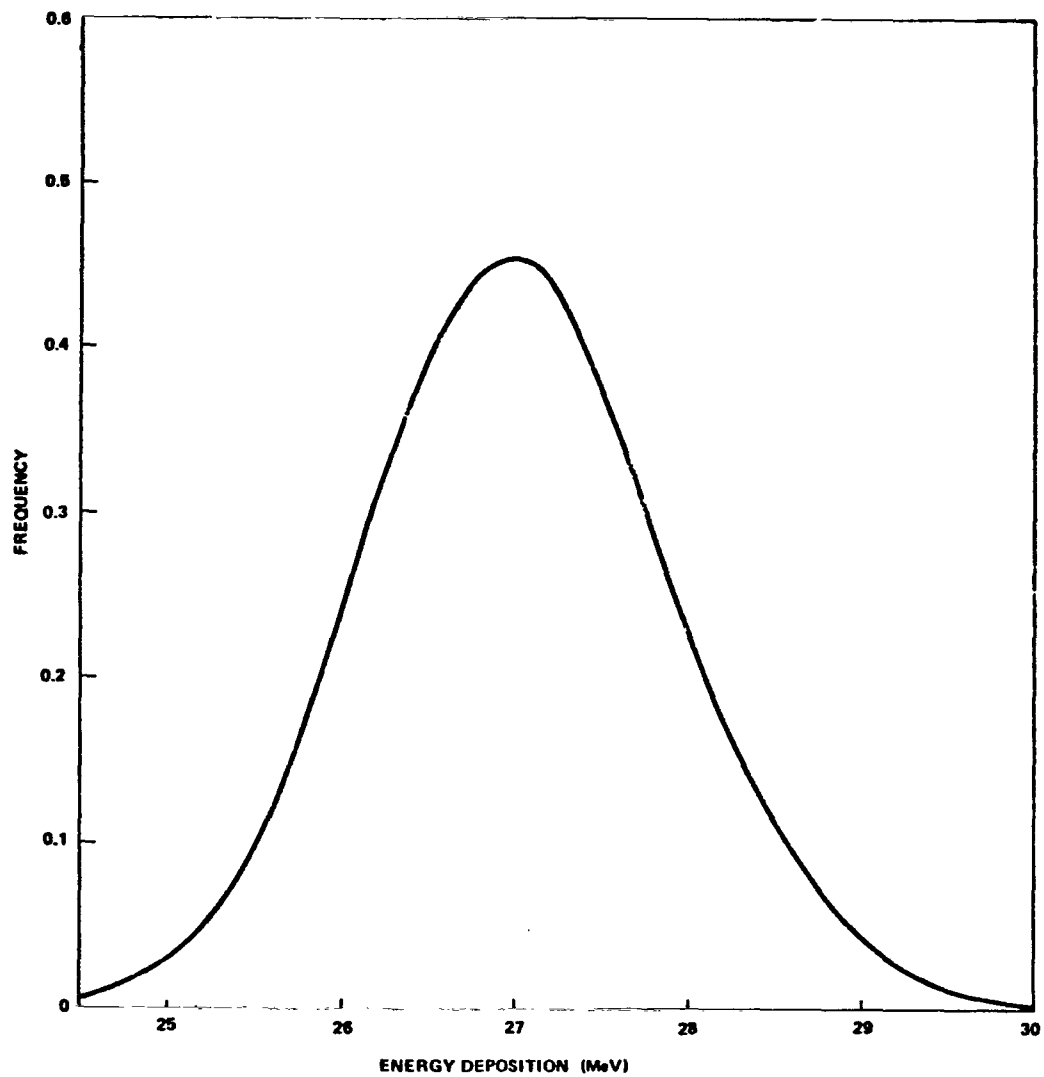


Figure 19. The energy deposition frequency distribution for chromium (Cr^{52}) nuclei normally incident at 10.0 GeV/nucleon on the four-chamber instrument. (These results are for the second two-chamber-coupled detector.)

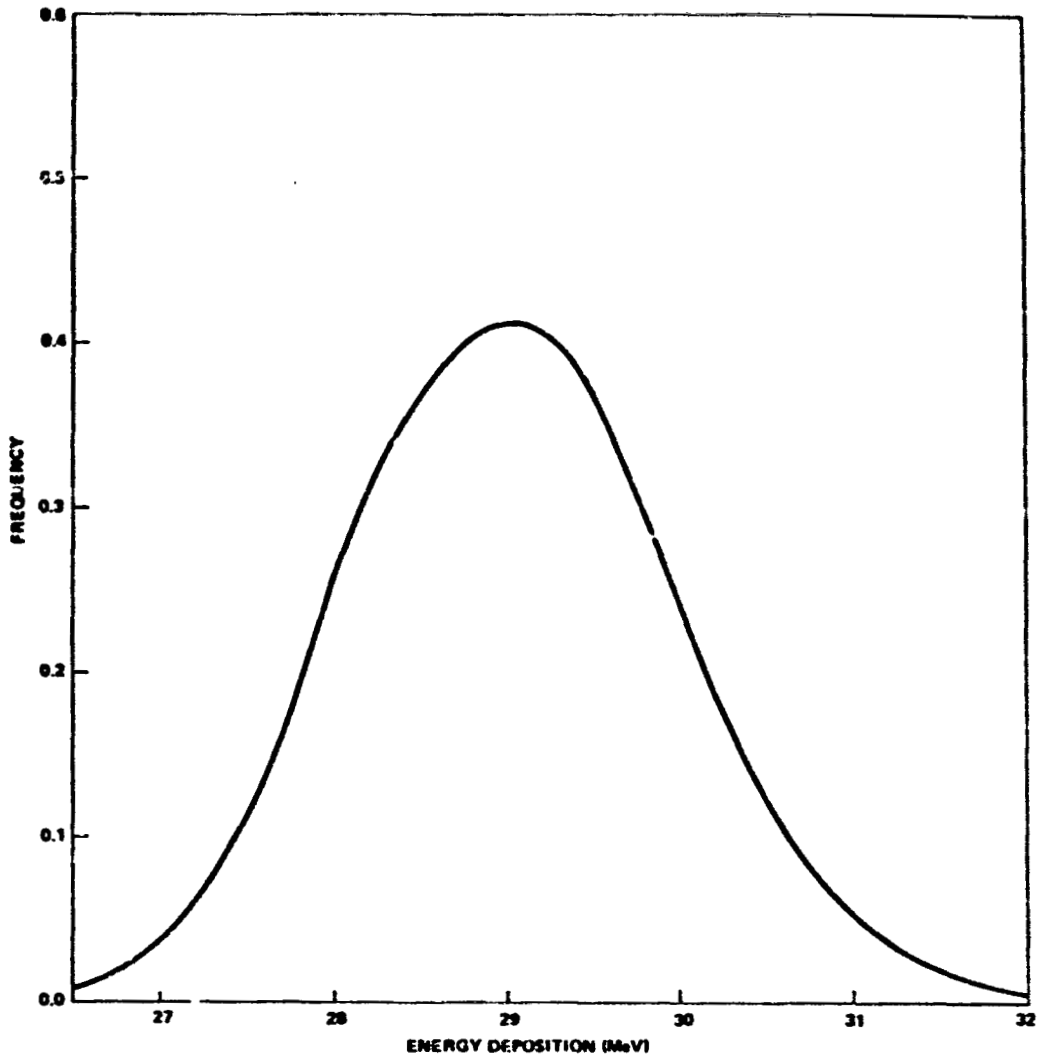


Figure 20. The energy deposition frequency distribution for manganese (Mn^{55}) nuclei normally incident at 10.0 GeV/nucleon on the four-chamber instrument. (These results are for the first two-chamber-coupled detector.)

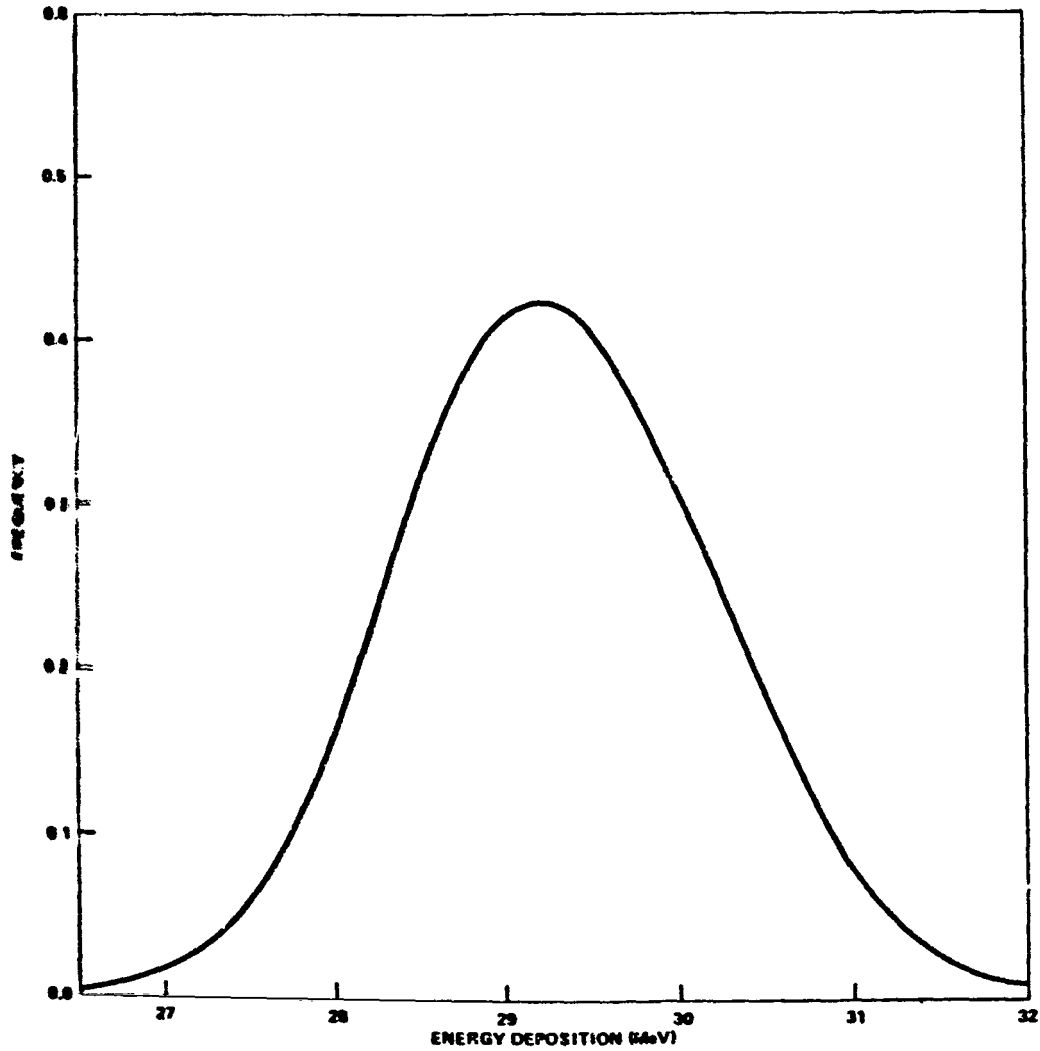


Figure 21. The energy deposition frequency distribution for manganese (Mn^{55}) nuclei normally incident at 10.0 GeV/nucleon on the four-chamber instrument. (These results are for the second two-chamber-coupled detector.)

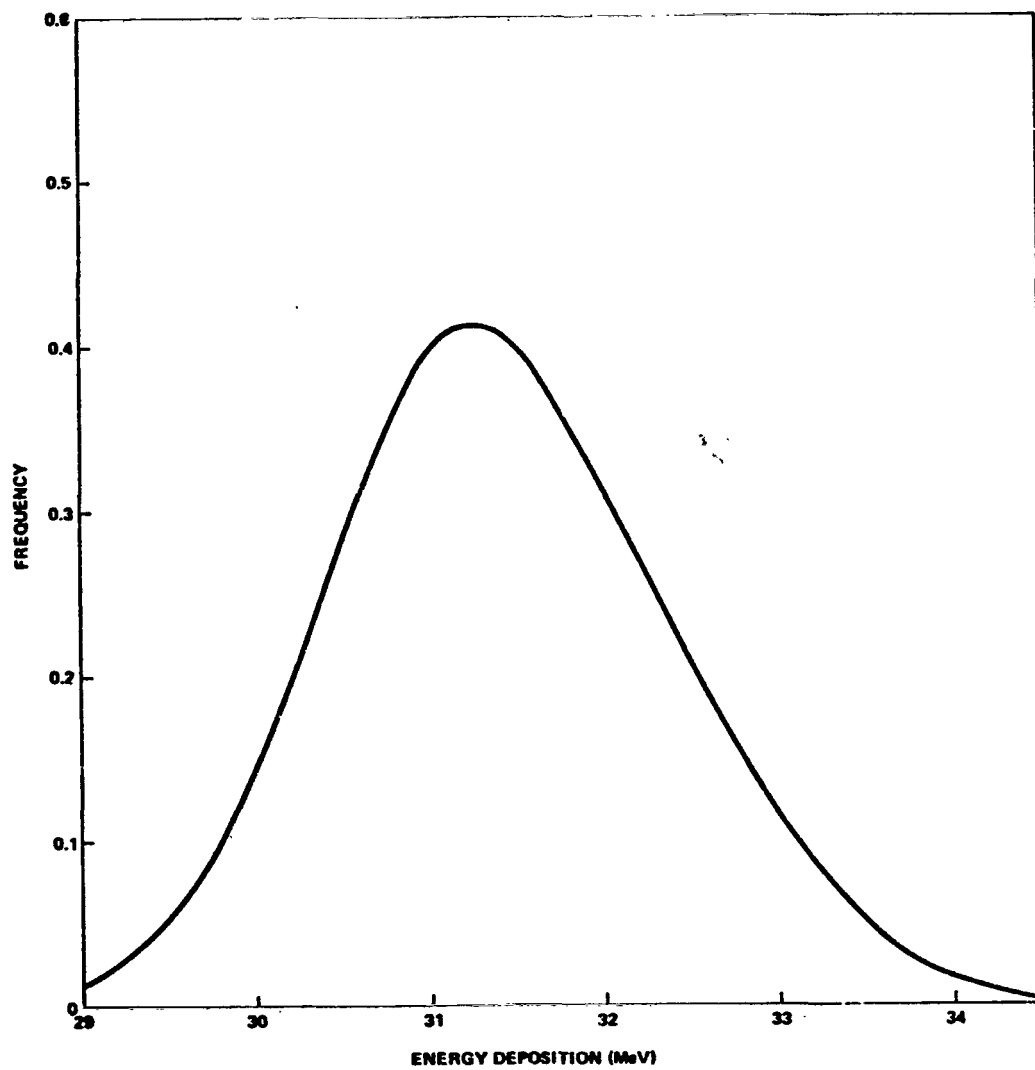


Figure 22. The energy deposition frequency distribution for iron (Fe^{56}) nuclei normally incident at 10.0 GeV/nucleon on the four-chamber instrument. (These results are for the first two-chamber-coupled detector.)

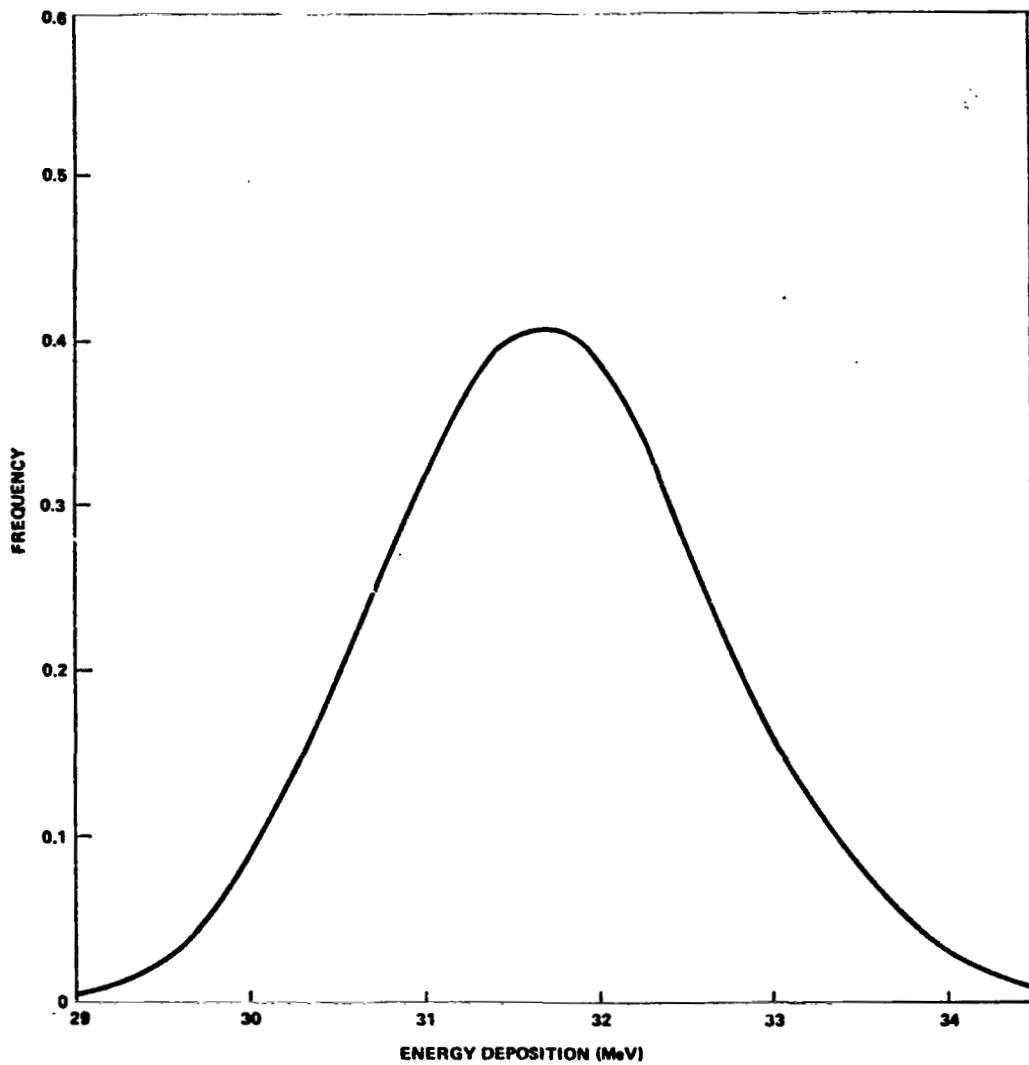


Figure 23. The energy deposition frequency distribution for iron (Fe^{56}) nuclei normally incident at 10.0 GeV/nucleon on the four-chamber instrument. (These results are for the second two-chamber-coupled detector.)

distribution is narrower because the high-energy delta rays basically tend to follow the primary particle's path through the instrument. First, they are initially produced at small angles from the direction of the primary path, and, second, the multiple scattering distribution for high-energy electrons is highly peaked in the forward direction. As they travel through the instrument, they deposit their initial energies over long segments of the primary particle's path, whereas in their production they have produced large fluctuations in the energy loss along short segments of the path. Because high-energy electrons produced above the chamber gas deposit more energy in the chamber gas than those high-energy electrons produced in the gas, reductions of the matter above the chamber should decrease the width of the energy deposition frequency distribution and slightly lower its mean energy deposition which could improve the instrument's charge resolution.

Presently, the calculation of energy deposition for charges around 20 and above are almost prohibitively expensive in terms of computer time because of the large number of delta rays involved. With careful reprogramming, the computer time can probably be reduced. For example, electrons cannot travel farther than their mean pathlength, assuming no straggling. Thus, electrons produced one pathlength from the chamber need not be considered in the calculation. The second improvement that needs to be introduced for extension of the calculation to very high charges is the introduction of the correct delta-ray production cross section from a partial wave calculation [3]. With these improvements, the method could cover the whole charge spectrum.

**APPENDIX A. DERIVATION OF THE ANGLE - ENERGY
RELATIONSHIP FOR DELTA-RAY PRODUCTION AND
THE EQUATION FOR MAXIMUM TRANSFERABLE ENERGY**

The initial relativistic momentum of the primary particle is given by

$$\vec{P} = \gamma M \vec{V} \tag{A-1}$$

where \vec{V} is its velocity, γ is given by

$$\gamma = \frac{1}{\sqrt{1 - \beta^2}} \tag{A-2}$$

and M is its mass. Conservation of momentum gives

$$\vec{P} = \vec{P}' + \vec{P}_e \tag{A-3}$$

where \vec{P}' is the primary particle momentum and \vec{P}_e is the delta-ray momentum. Assuming that the primary particle was initially traveling along the X axis in the positive X direction, we may write equation (A-3) in component form as

$$P = P' \cos \phi + P_e \cos \theta \tag{A-4}$$

$$0 = P' \sin \phi + P_e \sin \theta \tag{A-5}$$

where ϕ is the polar angle of P' and θ is the polar angle of P_e . Since delta rays are less massive than nuclei, $\cos \phi$ is always greater than zero, and we may use the identity $\cos^2 \phi + \sin^2 \phi = 1$ together with equation (A-5) to obtain

$$\cos \phi = \sqrt{1 - \frac{P_e^2}{P'^2} \sin^2 \theta} \tag{A-6}$$

Thus, equation (A-4) becomes

$$P = P' \sqrt{1 - \frac{P_e^2}{P'^2} \sin^2 \theta} + P_e \cos \theta \quad (\text{A-7})$$

Using algebra and the identity $\cos^2 \theta + \sin^2 \theta = 1$, we get

$$\cos \theta = \frac{P^2 - P'^2 + P_e^2}{2PP_e} \quad (\text{A-8})$$

Using conservation of energy momentum

$$E_i^2 = P_i^2 c^2 + M_i^2 c^4$$

and the momentum-energy relationship

$$P_i = \frac{\beta_i E_i}{c}$$

where E_i is the total energy, equation (A-8) becomes

$$\cos \theta = \frac{E^2 - E'^2 + E_e^2 - m^2 c^4}{2E\beta \sqrt{E_e^2 - m^2 c^4}} \quad (\text{A-9})$$

where E is the initial primary particle total energy, E' is the final primary particle total energy, E_e is the delta-ray total energy, and m is the electron mass. Using conservation of energy

$$E = E' + E_e - mc^2$$

equation (A-9) becomes

$$\cos \theta = \frac{E + mc^2}{E\beta} \sqrt{\frac{E_e - mc^2}{E_e + mc^2}} \quad (\text{A-10})$$

Using the mass energy relationship

$$E = \gamma Mc^2$$

and the definition of kinetic energy

$$\epsilon = E_e - mc^2 \quad ,$$

equation (A-10) becomes

$$\cos \theta = \frac{1 + \frac{m}{M\gamma}}{\beta} \sqrt{\frac{\epsilon}{\epsilon + 2mc^2}} \quad (\text{A-11})$$

For $m/M \ll 1$, equation (A-11) is approximately

$$\cos \theta \approx \frac{1}{\beta} \sqrt{\frac{\epsilon}{\epsilon + 2mc^2}} \quad (\text{A-12})$$

Solving equation (A-11) for ϵ we get

$$\epsilon = \frac{2mc^2 \beta^2 \cos^2 \theta}{\left(1 + \frac{m}{M\gamma}\right)^2 - \beta^2 \cos^2 \theta} \quad (\text{A-13})$$

The maximum energy transfer occurs when θ is zero; thus,

$$\epsilon_{\max} = \frac{2 mc^2 \beta^2}{\left(1 + \frac{m}{M\gamma}\right)^2 - \beta^2}$$

or squaring the bottom term and simplifying

$$\epsilon_{\max} = \frac{2 mc^2 \beta^2 \gamma^2}{1 + \frac{2m\gamma}{M} + \frac{m^2}{M^2}} \quad (A-14)$$

where $m/M \ll 1$

$$\epsilon_{\max} \approx 2mc^2 \beta^2 \gamma^2 \quad (A-15)$$

APPENDIX B. SAMPLING FROM FREQUENCY DISTRIBUTION

A continuous frequency distribution $f(X)$, often called the density function, is defined such that $f(X)dX$ gives the probability of an observation between X and $x + dX$. The cumulative frequency distribution is defined as

$$F(X) = \int_{-\infty}^X f(X') dX' \quad (B-1)$$

It gives the probability of finding an observation X' less than or equal to X . For discrete frequency distributions, the cumulative distribution is given by

$$F(X_N) = \sum_{j=0}^N P(X_j) \quad (B-2)$$

where $P(X_j)$ is the probability of observing X_j . Obviously, $F(X)$ varies between zero and unity.

All sampling in these calculations is based on one simple rule [24]: To obtain a sample whose frequency distribution approximates a given continuous frequency distribution, the equation

$$F(X_R) = R \quad (B-3)$$

is solved for X_R the sampled variable where R is a pseudorandom number uniformly distributed on the interval 0 to 1. For a discrete distribution, the inequality

$$F(X_{RN}) \geq R > F(X_{RN-1}) \quad (B-4)$$

is solved for X_{RN} .

The pseudorandom number R is generated using the multiplicative congruence method. Given the last pseudorandom interger N_1 between 1 and $2^{35} - 1$, the next interger in the sequence is given by

$$N_I + 1 = 5^{15} N_I \text{ mod } 2^{35}$$

and

$$R = \frac{N_I + 1}{2^{35}} \quad (\text{B-5})$$

As an example of sampling from a continuous distribution, consider the frequency distribution of the energy of high-energy delta rays given in equation (21). The cumulative distribution is given by

$$F(\epsilon_R) = \frac{\frac{1}{\epsilon_1} - \frac{1}{\epsilon_R} + \frac{\beta^2}{\epsilon_{\max}} \ln \frac{\epsilon_1}{\epsilon_R}}{\frac{1}{\epsilon_1} - \frac{1}{\epsilon_{\max}} + \frac{\beta^2}{\epsilon_{\max}} \ln \frac{\epsilon_1}{\epsilon_{\max}}}$$

Thus, we have from equation (B-3)

$$R = \frac{\frac{1}{\epsilon_1} - \frac{1}{\epsilon_R} + \frac{\beta^2}{\epsilon_{\max}} \ln \frac{\epsilon_1}{\epsilon_R}}{\frac{1}{\epsilon_1} - \frac{1}{\epsilon_{\max}} + \frac{\beta^2}{\epsilon_{\max}} \ln \frac{\epsilon_1}{\epsilon_{\max}}}$$

which can be solved numerically for ϵ_R by the simple iteration

$$\epsilon_{Ri} = \left[\frac{1}{\epsilon_1} + \frac{\beta^2}{\epsilon_{\max}} \ln \frac{\epsilon_1}{\epsilon_{Ri-1}} - R \frac{1}{\epsilon_1} - \frac{1}{\epsilon_{\max}} + \frac{\beta^2}{\epsilon_{\max}} \ln \frac{\epsilon_1}{\epsilon_{\max}} \right]^{-1}$$

Where the initial guess ϵ_{R1} is taken as ϵ_1 , convergence is rapid except at ϵ_{\max} .

APPENDIX C. THE MOLIERE MULTIPLE SCATTERING DISTRIBUTION

The Moliere multiple scattering distribution gives the angular distribution expected for a beam of electrons which has been scattered several times (>20). Bethe [21] provides an easily understood description of the distribution. It is given by

$$M(\theta) \theta d\theta = \Psi d\Psi \left(2e^{-\Psi} + \frac{M^{(2)}(\Psi)}{B} + \frac{M^{(2)}(\Psi)}{B^2} + \dots \right) \quad (C-1)$$

where $M(\theta)$ is the frequency of scattering through the angle θ . The series is sufficiently accurate when terminated with the terms shown [21]. The functions $M^{(1)}(\theta)$ and $M^{(2)}(\theta)$ are tabulated by Bethe [21]. The parameter B is defined by the transcendental equation

$$B - \ln B = b \quad (C-2)$$

where b is given by

$$b = \ln \frac{\chi_c^2}{1.167 \chi_a^2}$$

χ_a is the screening angle given by

$$\chi_a = \frac{\hbar}{0.885 a_0 Z_o^{-1/3} P_e} \sqrt{1.13 + 3.76 \frac{Z_o}{137 \beta_e}} \quad (C-3)$$

where \hbar is Planck's constant divided by 2π , a_0 is the Bohr radius, Z_o is the atomic number of the material, P_e is the magnitude of the electron's momentum, and β_e is the magnitude of the electron's speed over the speed of light. χ_c is given by

$$\chi_c = \frac{2e^2}{P_e \beta_e c} \sqrt{\pi N_a \Delta X_1 Z_o (Z_o + 1)} \quad (C-4)$$

where N_a is that atomic density (atoms/cm³). Ψ is defined by

$$\Psi \equiv \frac{\theta}{\chi_c \sqrt{B}} \quad (C-5)$$

Since the electron energy changes in passing through ΔX_I , the mean energy $(\epsilon_I + \epsilon_{I-1})/2$ is used to define P_e and β_e . Equation (C-2) is solved numerically for B by the simple iteration

$$B_{i+1} = b + \ln B_i \quad (C-6)$$

The initial guess B_1 for the initial scatter is 8.0. For succeeding scatters, the converged result from the previous scatter is used for the initial guess. Convergence to several places is usually obtained in five or six iterations of equation (C-6).

Sampling from equation (C-1), we use equation (B-3) or

$$\int_0^{\theta_R} M(\theta) \theta d\theta = R \quad (C-7)$$

which reduces to

$$e^{-\Psi_R^2} + \frac{\int_0^{\Psi_R} M^{(1)}(\Psi) \Psi d\Psi}{B} + \frac{\int_0^{\Psi_R} M^{(2)}(\Psi) \Psi d\Psi}{B^2} = R \quad (C-8)$$

where, from equation (C-5),

$$\theta_R = \chi_c \sqrt{B} \Psi_R$$

The integrals in equation (C-8) are performed numerically to the tabulated values given in Reference 21. Since the exponential is the most important term on the right of equation (C-8), an initial guess at Ψ_R is obtained by solving the equation

$$\Psi'_R = -\ln \sqrt{R} \quad .$$

Then, the correct value is found by searching through the tabulated values of the integral from Ψ' . Linear interpolation is used between tabulated values.

APPENDIX D. USE OF DIRECTION COSINES FOR DESCRIBING PARTICLE SCATTERING

One of the most efficient ways of describing particle's direction for the Monte-Carlo transport is the use of direction cosines. In Cartesian coordinates, a unit vector along the particle path is given by

$$\mathbf{k}' = \alpha \mathbf{i} + \beta \mathbf{j} + \gamma \mathbf{k} \quad (\text{D-1})$$

where α , β , and γ are the X-, Y-, and Z-direction cosines, respectively. The utility of this method is shown by the calculation of the new particle coordinates when the particle has moved a distance r . The new coordinates are given by

$$X_1 = X_0 + \alpha r$$

$$Y_1 = Y_0 + \beta r$$

$$Z_1 = Z_0 + \gamma r$$

where X_0 , Y_0 , and Z_0 are the old coordinates. The problem arises in determining the new direction cosines when a particle scatters at some angle θ' from the original direction.

If we define a new coordinate system with its positive Z axis directed along \mathbf{k}' and its X axis directed along \mathbf{i}' where \mathbf{i}' is defined by

$$\mathbf{i}' \equiv \frac{\mathbf{k}' \times \mathbf{k}}{|\mathbf{k}' \times \mathbf{k}|} \quad (\text{D-2})$$

Since

$$\mathbf{k}' \times \mathbf{k} = \begin{pmatrix} \mathbf{i} & \mathbf{j} & \mathbf{k} \\ \alpha & \beta & \gamma \\ 0 & 0 & 1 \end{pmatrix} = \beta \mathbf{i} - \alpha \mathbf{j} \quad ,$$

equation (D-2) becomes

$$i' = \frac{\beta}{\sqrt{\alpha^2 + \beta^2}} i - \frac{\alpha}{\sqrt{\alpha^2 + \beta^2}} j \quad . \quad (D-3)$$

For a right-hand coordinate system,

$$j' = \frac{k' \times i'}{|k' \times i'|}$$

Since k' and i' are perpendicular, the magnitude of the cross product is one and

$$j' = \frac{1}{\sqrt{\alpha^2 + \beta^2}} [\alpha \gamma i + \beta \gamma j - (\alpha^2 + \beta^2) k] \quad . \quad (D-4)$$

Now if we have a unit vector in the new system given by

$$\hat{n} = \alpha' i' + \beta' j' + \gamma' k' \quad , \quad (D-5)$$

it is given in the unprimed system by

$$\begin{aligned} n &= \alpha' \frac{1}{\sqrt{\alpha^2 + \beta^2}} (\beta i - \alpha j) \\ &+ \beta' \frac{1}{\sqrt{\alpha^2 + \beta^2}} [\alpha \gamma i + \beta \gamma j - (\alpha^2 + \beta^2) k] \\ &+ \gamma' [\alpha i + \beta j + \gamma k] \end{aligned}$$

or regrouping

$$\begin{aligned}
\mathbf{n} &= \frac{\alpha' \beta + \beta' \alpha \gamma}{\sqrt{\alpha^2 + \beta^2}} + \gamma' \alpha \mathbf{i} \\
&+ \frac{-\alpha' \alpha + \beta' \beta \gamma}{\sqrt{\alpha^2 + \beta^2}} + \gamma' \beta \mathbf{j} \\
&+ -\beta' \sqrt{\alpha^2 + \beta^2} + \gamma' \gamma \mathbf{k} .
\end{aligned}$$

Thus, the direction cosines of \mathbf{n} in the old system are

$$\begin{aligned}
\alpha^* &= \frac{\alpha' \beta + \beta' \alpha \gamma}{\sqrt{\alpha^2 + \beta^2}} + \gamma' \alpha \\
\beta^* &= \frac{-\alpha' \alpha + \beta' \beta \gamma}{\sqrt{\alpha^2 + \beta^2}} + \gamma' \beta \\
\gamma^* &= -\beta' \sqrt{\alpha^2 + \beta^2} + \gamma' \gamma .
\end{aligned} \tag{D-6}$$

We note that the direction cosine in the new system α' , β' , γ' are related to the scattered angles by

$$\begin{aligned}
\alpha' &= \cos \phi' \sin \theta' \\
\beta' &= \sin \phi' \sin \theta' \\
\gamma' &= \cos \theta' ,
\end{aligned} \tag{D-7}$$

where ϕ' is the azimuthal scattering angle and θ' is the polar scattering angle.

**APPENDIX E. DERIVATION OF THE CONTINUITY EQUATION
OF THE ENERGY-LOSS FREQUENCY DISTRIBUTION**

Let $\phi(X, \Delta)$ be the flux of particles that having passed through a distance X of material have lost energy Δ and let $P(\Delta X, \Delta' \rightarrow \Delta)$ be the probability that a particle with energy loss Δ' at X will have an energy loss Δ after passing through an additional distance ΔX of material where only interactions that result in energy losses below ϵ_1 are considered to contribute to total energy losses Δ or Δ' . Then the flux $\phi(X + \Delta X, \Delta)$ is given by

$$\begin{aligned} \phi(X + \Delta X, \Delta) = & \phi(X, \Delta) + \int_0^{\Delta} P(\Delta X, \Delta' \rightarrow \Delta) \phi(X, \Delta') d\Delta' \\ & - \int_{\Delta}^{\infty} P(\Delta X, \Delta \rightarrow \Delta'') \phi(X, \Delta) d\Delta'' \end{aligned} \quad (E-1)$$

where the first integral on the right is because of particles scattered into Δ and the second integral is because of particles scattered out of Δ . Since

$$\frac{\partial \phi(X, \Delta)}{\partial X} = \lim_{\Delta X \rightarrow 0} \frac{\phi(X + \Delta X, \Delta) - \phi(X, \Delta)}{\Delta X}$$

using equation (E-1) we obtain

$$\begin{aligned} \frac{\partial \phi(X, \Delta)}{\partial X} = \lim_{\Delta X \rightarrow 0} \left[\int_0^{\Delta} \frac{P(\Delta X, \Delta' \rightarrow \Delta)}{\Delta X} \phi(X, \Delta') d\Delta' \right. \\ \left. - \int_{\Delta}^{\infty} \frac{P(\Delta X, \Delta \rightarrow \Delta'')}{\Delta X} \phi(X, \Delta) d\Delta'' \right] \end{aligned} \quad (E-2)$$

Since we are considering only interaction which results in losses below energy ϵ_1 in the limit of small ΔX , $P(\Delta X, \Delta' \rightarrow \Delta)$ is zero for $\Delta' \rightarrow \Delta > \epsilon_1$ and we may change the limits on the integrals in equation (E-2) accordingly. Thus,

$$\frac{\partial \phi(X, \Delta)}{\partial X} = \int_B^{\Delta} \omega(E, \Delta - \Delta') \phi(X, \Delta') d\Delta' - \int_{\Delta}^{\Delta + \epsilon_1} \omega(E, \Delta'' - \Delta) \phi(X, \Delta) d\Delta''$$

where

$$B = \begin{cases} \Delta - \epsilon_1 & \Delta > \epsilon_1 \\ 0 & \Delta < \epsilon_1 \end{cases} \quad (E-3)$$

Letting $\epsilon = \Delta - \Delta'$, $\epsilon'' = \Delta'' - \Delta$, and $b = \Delta - B$, we obtain

$$\frac{\partial \phi(X, \Delta)}{\partial X} = \int_0^b \omega(E, \epsilon) \phi(X, \Delta - \epsilon) d\epsilon - \int_0^{\epsilon_1} \omega(E, \epsilon'') \phi(X, \Delta) d\epsilon'' \quad (E-4)$$

The probability density function $f(X, \Delta)$ is given by

$$f(X, \Delta) = \frac{\phi(X, \Delta)}{\int_0^E \phi(X, \Delta') d\Delta'} \quad (E-5)$$

Thus, the continuity equation of $f(X, \Delta)$ is found by dividing both sides of equation (E-4) by $\int_0^E \phi(X, \Delta') d\Delta'$, yielding

$$\frac{\partial f(X, \Delta)}{\partial X} = \int_0^b \omega(E, \epsilon) f(X, \Delta - \epsilon) d\epsilon - \int_0^{\epsilon} \omega(E, \epsilon') f(X, \epsilon') d\epsilon' \quad . \quad (E-6)$$

George C. Marshall Space Flight Center
National Aeronautics and Space Administration
Marshall Space Flight Center, Alabama 35812, October 13, 1972
832-89-00

REFERENCES

1. Epstein, J.W., Fernandez, J.I., Israel, M.H., Klarmann, J., and Mewaldt, R.A.: Nuclear Instruments and Methods. 95, 77, 1971.
2. Fowler, P.H., Chapham, V.M., Cowen, V.G., Kidd, J.M., and Moses, R.T.: Proc. Roy. Soc. London, A318, 1, 1970.
3. Eby, P.B., and Morgan, S.H., Jr.: Phys. Rev. 3a, June 1972.
4. Semikoff, V.B.: J. Exp. Theo. Phys. Lett. 9, 324, 1969.
5. Landau, L.D.: J. Phys. USSR 8, 204, 1944.
6. Symon, K.R.: Fluctuations in Energy Loss by High Energy Charged Particles in Passing Through Matter. Thesis, Harvard University, 1949.
7. Vavilov, P.V.: Soviet Physics. JETP 5, 749, 1957.
8. Segre, E.: Nuclei and Particles. W.A. Benjamin, Inc., New York, 1965.
9. Sternheimer, R.M.: Phys. Rev. 91, 256, 1953.
10. Cleshorn, T.F., Freier, P.S., and Waddington, C.J.: Canadian Journal of Physics. 46, S573, 1968.
11. Uehlung, E.A.: Annual Review of Nuclear Science. 4, 315, 1954.
12. Livingston and Bethe: Rev. Mod. Phys. 9, 245, 1937.
13. Lebedev, N.N.: Special Functions and Their Applications. Prentice Hall, Inc., Englewood Cliffs, New Jersey, 1965.
14. Hill, C.W., Ritchie, W.B., and Simpson, K.M.: Data Compilation and Evaluation of Space Shielding Problems, Volume 1. Lockheed Report ER 7777, April 1966.
15. Feller, W.: An Introduction to Probability Theory and Its Applications, Volume 2. John Wiley & Sons, Inc., New York, 1957.
16. Berger, M.J.: Methods in Computational Physics, Volume 1. Academic Press, Inc., New York, 135-215, 1963.
17. Perkins, J.F.: Phys. Rev. 126, 1781, 1962.
18. Berger, M.J., and Seltzer, S.M.: Tables of Energy Losses and Ranges of Electrons and Positrons. NASA Report SP-3012, 1964.

REFERENCES (Concluded)

19. Moliere, Von Gert: *Z. Naturforschg.* 2a, 133, 1947.
20. Moliere, Von Gert: *Z. Naturforschg.* 3a, 78, 1948.
21. Bethe, H.A.: *Phys. Rev.* 89, 1256, 1953.
22. Watts, J.W., and Burrell, M.O.: *Electron and Bremsstrahlung Penetration and Dose Calculation.* NASA TN D-6385, June 1971.
23. Viswanathan, S.P., Mace, R., and Palmatier, E.D.: *Il Nuovo Cimento.* 28, 850, 1963.
24. Ormes, J.F., Balasubrahanyan, V.K., Bowen, T., Huggett, R.W., Parnell, T.A., and Pinkau, K.: *A Proposal for an Orbital Laboratory for the HEAO.* NASA/GSFC X-661-71, January 1971.
25. Goertzel, G., and Kalos, M.H.: *Progress in Nuclear Energy, Series I, Volume II.* 315-369, Pergamon Press, New York, 1958.

END

DATE

FILMED

APR 11 1973